2007

Destabilization and characterization of LiBH4/MgH2 complex hydride for hydrogen storage

Luis A. Rivera
University of South Florida

Destabilization and Characterization of $LiBH_4/MgH_2$ Complex Hydride for Hydrogen Storage

by

Luis A. Rivera

A thesis submitted in partial fulfillment
of the requirements for the degree of
Master of Science in Chemical Engineering
Department of Chemical Engineering
College of Engineering
University of South Florida

Major Professor: John T. Wolan, Ph.D.
Elias Stefanakos, Ph.D.
Aydin K. Sunol, Ph.D.
Sesha Srinivasan, Ph.D.

Date of Approval:
April 9, 2007

Keywords: Hydrogen Desorption, Lithium Borohydride, Magnesium Hydride, Dehydrogenation, Mechano-Chemical Process, Dopants

DEDICATION

Dedicated to my family, my lovely wife Ileanexis, my daughter Adriana and my fellow engineers…

May God bless them.

ACKNOWLEDGEMENTS

I would like to thank my advisors and co-advisors Dr. John Wolan, Dr. Elias Stefanakos, Dr. Aydin Sunol and Dr. Sesha Srinivasan for their support, guidance and advice provided over the course of my research experience here at USF. I would also like to thank Matt Smith, Rob Tufts, Jay Bieber and Michael Jurczyk for the analytical training and advice.

I, gratefully acknowledge my friends Carla Webb, Cecil Coutinho, Jonathan Mbah, Eric Weaver, Diego Escobar and Ajay Vidyasagar for their constant support throughout the learning process. I would also like to thank Mr. Bernard Batson, Dr. Ashanti J. Pyrtle, Dr. Shekhar Bhansali, the National Science Foundation's Bridge to Doctorate program and the US Department of Energy's Hydrogen Fuel Initiative (HFI) program for the financial support. Last, but not least, I wish to acknowledge my family for their encouragements and moral support in every step of my academic career.

TABLE OF CONTENTS

LIST OF TABLES

LIST OF FIGURES

DESTABILIZATION AND CHARACTERIZATION OF $LiBH_4/MgH_2$ COMPLEX HYDRIDE FOR HYDROGEN STORAGE

Luis A. Rivera

ABSTRACT

The demands on Hydrogen fuel based technologies is ever increasing for substitution or replacing fossil fuel due to superior energy sustainability, national security and reduced greenhouse gas emissions. Currently, the polymer based proton exchange membrane fuel cell (PEMFC), is strongly considered for on-board hydrogen storage vehicles due to low temperature operation, efficiency and low environmental impact. However, the realization of PEMFC vehicles must overcome the portable hydrogen storage barrier. DOE and FreedomCAR technical hydrogen storage targets for the case of solid state hydrides are: (1) volumetric hydrogen density > 0.045 kgH_2/L, (2) gravimetric hydrogen density > 6.0 wt%, (3) operating temperature < 150^oC, (4) life-times of 1000 cycles, and (5) a fast rate of H_2 absorption and desorption.

To meet these targets, we have focused on lithium borohydride systems; an alkali metal complex hydride with a high theoretical hydrogen capacity of 18 wt.%. It has been shown by Vajo et al. that adding MgH_2, improves the cycling capacity of $LiBH_4$. The pressure-composition-isotherms of the destabilized $LiBH_4 + MgH_2$ system show an extended plateau pressure around 4-5 bars at 350°C with a good cyclic stability. The mentioned destabilizing mechanism was successfully utilized to synthesize the complex

hydride mixture $LiBH_4$ + ½MgH_2 + Xmol% $ZnCl_2$ catalyst (X=2, 4, 6, 8 and 10) by ball milling process. The added $ZnCl_2$ exhibited some mild catalytic activity which resulted in a decomposition temperature reduction to 270°C. X-ray powder diffraction profiles exhibit LiCl peaks whose intensity increases proportionately with increasing $ZnCl_2$ indicating an interaction between catalyst and hydride system, possibly affecting the total weight percent of desorbed hydrogen. Thermal gravimetric analysis profiles for MgH_2 + 5mol% nanoNi and $LiBH_4$ + $ZnCl_2$ + 3mol% nanoNi indicate that small concentrations of nano-nickel acts as an effective catalyst that reduces the mixture desorption temperature to around 225^{o}C and 88^{o}C, respectively. Future work will be focused on thermodynamic equilibrium studies (PCT) on the destabilized complex hydrides.

CHAPTER 1

INTRODUCTION

1.1 Current Energy "Situation"

Our current energy "situation" has been the main motivator to pursue research in metal hydrides for on-board hydrogen storage. This "situation" has been created by several factors threatening to destabilize our economy, environment and national energy security if not solved or at least tackled "on time". A possible key factor is closely related to our oil dependency and its influence. However, there are multiple solutions that could reduce our oil dependency while at the same time re-stabilizing the economy, improving the environment and strengthening our national energy security. This section will briefly discuss how our oil dependency plays its role and possible alternatives.

1.1.1 Oil Market

Note from the author: "Most of the data presented in this section 1.1.1 Oil Market was taken from the Energy Information Administration (EIA) which is the Official Energy Statistics from the United States government".

For decades the world, mostly the United States, enjoyed the access to relatively inexpensive and abundant crude oil (fossil fuels) supply. In 2005, the United States energy consumption reached the 99.9 quadrillion Btu and a petroleum consumption of

21 million barrels per day. In addition, around 63% of the United States energy sources relied on fossil fuels to cover its demand in 2005 [1]. According to EIA data [2], for the third quarter of 2006, the United States oil demand (around 20.80 millions barrels per day) has surpassed its oil supply (approx. 8.48 millions barrels per day) reaching deficits levels higher than 2 times its supply. If the United States decides to use its own reserves, which are about 21.4 billions barrels (refer to Table 1.1) to supply its current demand, the reservoirs would be depleted in approximately 3 years, a possible reason to cover the deficit with foreign oil imports.

Table 1.1: World Oil Reserves by Country as of January 1, 2006 [3].

Country	Oil Reserves (Billions Barrels)
Saudi Arabia	264.3
Canada	178.8
Iran	132.5
Iraq	115.0
Kuwait	101.5
UAE	97.8
Venezuela	79.7
Russia	60.0
Libya	39.1
Nigeria	35.9
United States	21.4
China	18.3
Qatar	15.2
Mexico	12.9
Algeria	11.4
Brazil	11.2
Kazakhstan	9.0
Norway	7.7
Azerbaijan	7.0
India	5.8
Rest of World	68.1
World Total	1292.5

In a broader scope, a world supply of approximately 85.18 millions barrel per day barely suffices a total world consumption of approximately 84.22 millions barrel per day [2]. World reserves are estimated at 1292.5 billions barrels (refer to Figure1.1) [3], if considering constant world consumption the reserves life-span would be around 42 years.

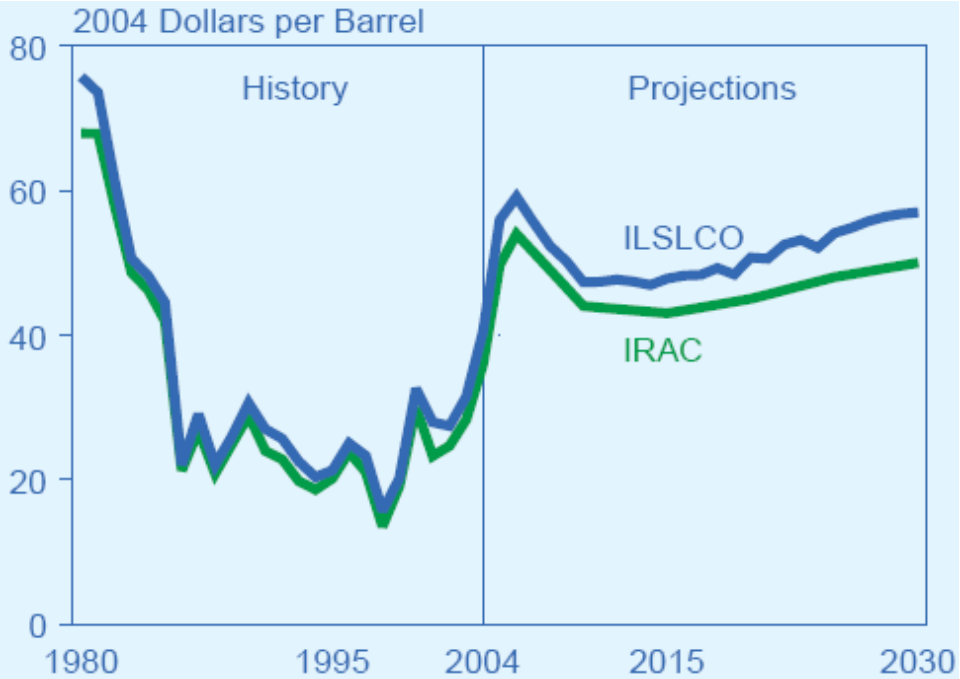

Figure 1.1: World Oil Prices, 1980-2030. Comparison of IRAC (Imported Refiner Acquisition Cost) and Average Price of Imported Low-Sulfur, Light Crude Oil (ILSLCO) to U.S. Refiners [6].

Estimated values for 2025, world oil consumption and total resources (the *resources* term counts: proved reserves, reserves growth and undiscovered reserves) were estimated at around 111 million barrels per day [4] and 2961.6 billion barrels [5], respectively. If by 2025, the estimate is real with no other possible reserves and a constant consumption, the world oil resources would disappeared in approximately 73 years close to the year 2100.

Additionally, according to a report from the EIA [6], world oil prices have been dramatically increasing since 1995 and are projected to stabilize by 2015 (refer to Figure 1.1). The increase in crude oil prices has increased U.S. retail gasoline prices which could reduce consumer purchase power and its accessibility (refer to Figure 1.2) [7].

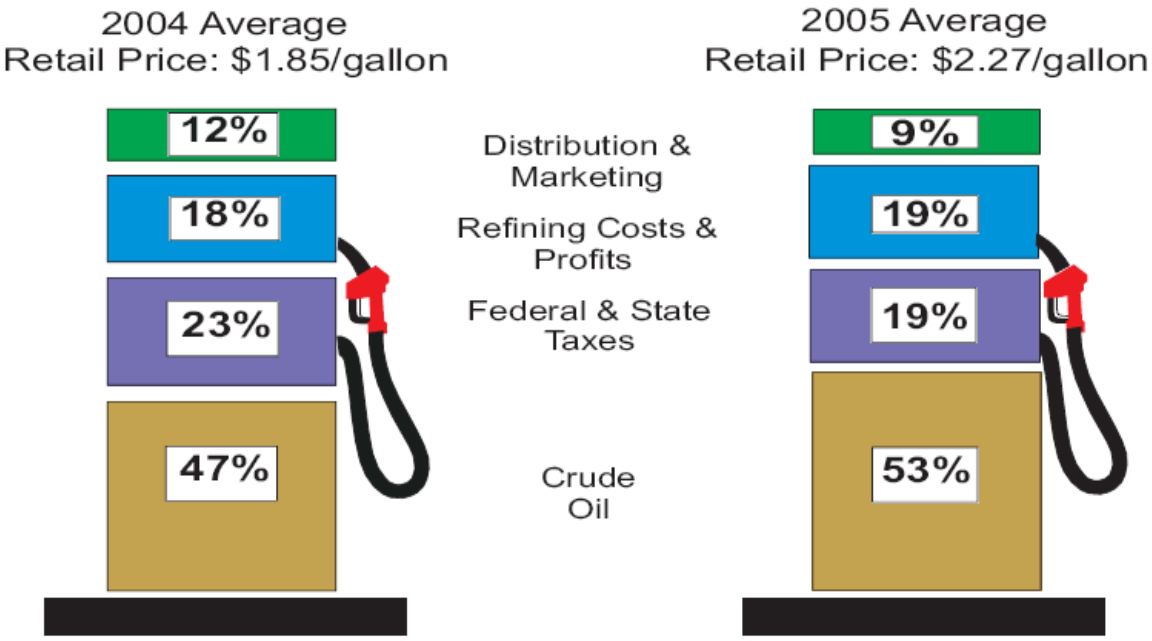

Figure 1.2: Price Comparison for a Gallon of Regular Grade Gasoline in 2004 and 2005 [7].

Our dependency and the oil market have critically affected our national security and economy however, not limited to those mentioned. The constant use of fossil fuels has also affected our environment locally and globally. The combustion of fossil fuels produces carbon dioxide (CO_2), a component directly linked to the greenhouse gases and global warming. The next section will briefly discuss the history and effect of carbon dioxide.

1.1.2 Global Warming and Greenhouse Effect

Scientists tried to explain the relationship between carbon dioxide effects of the global warming. The first steps to measure carbon dioxide levels in the atmosphere were still speculated until in 1960, when Keeling discovered that carbon dioxide levels in the atmosphere were increasing [8], (refer to Figure 1.3).

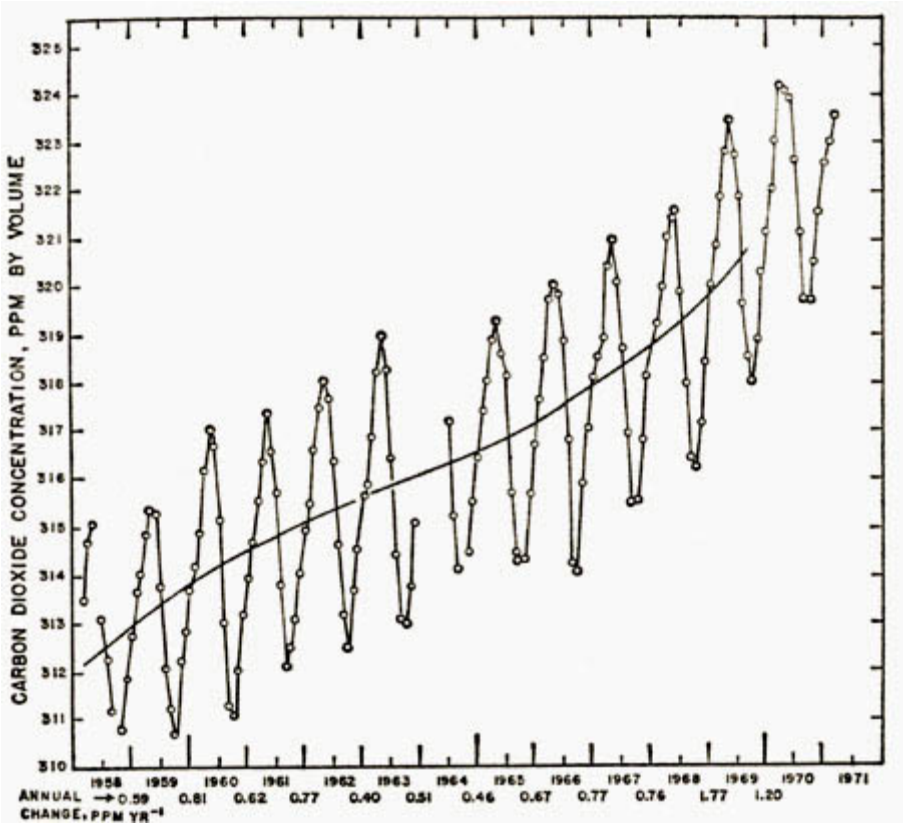

Figure 1.3: "Keeling Curve" – CO_2 Measurement at Mauna Loa, Hawaii [9].

However, the plot only indicates the increasing carbon dioxide levels in the atmosphere and not a direct relationship with temperature (greenhouse effect) and atmospheric carbon dioxide levels. Close to 1985, scientists' studying Antarctic ice cores found a direct relationship of temperature with concentration of carbon dioxide levels for past ice age cycles (see Figure 1.4) [10].

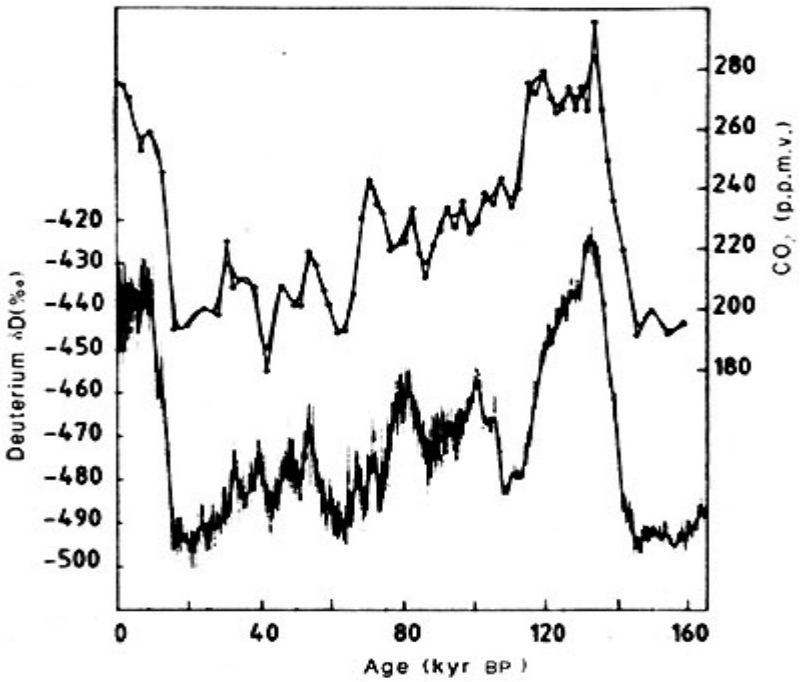

Figure 1.4: CO_2 Concentration in Parts Per Million Plotted Against Thousands of Years Before Present [11].

This finding demonstrated that carbon dioxide takes an important role in our global climate. In addition, further investigations have found that carbon dioxide levels are increasing [12]. According to an EIA report, it has been projected that world carbon dioxide emissions increases from 21,223 million metric tons in 1990 to 43,676 million metric tons by 2030 [13]. The continuous and increased use of carbon base energy sources, in these case fossil fuels, could further catalyze the already affected global climate by the addition of more anthropogenic carbon dioxide. Climate changes and limited oil availability threat to inflict worldwide damage with irreversible consequences if solutions of a significant magnitude are not implemented. Several these solutions are non-carbon (fossil fuels) base power sources which are currently in use throughout the world, aiding the task reducing the use of fossil fuels however; these non-carbon base technologies also face limitations.

1.1.3 The Alternative

Current technological advances are providing the world with the solution to our oil dependency. Technologies such as: nuclear energy, wind energy, hydropower and solar energy has been in use for several years in many countries to supply the demand for energy, while reducing oil consumption and carbon dioxide generation. On the other hand, fully implementing these new technologies has proven to be a difficult task due to their intrinsic limitations [14], which would not be discussed in this report. Recent global factors have motivated multiple countries, including the United States, to consider PEM (Proton Exchange Membranes) fuel cells (see Figure 1.5) as future source of energy, in the what would be called the *hydrogen economy*, due to their high efficiency, negligible air pollution and versatility [15, 16]. Despite the PEM positive qualities and the significant impact it will bring to the hydrogen economy, the *hydrogen storage* limitation must be solved in order to achieve the goal. In this report it is focused on the analysis and characterization of complex light weight metal hydrides for on-board hydrogen storage. The main objectives of the research are based on the technical targets set by the US Department of Energy (DOE).

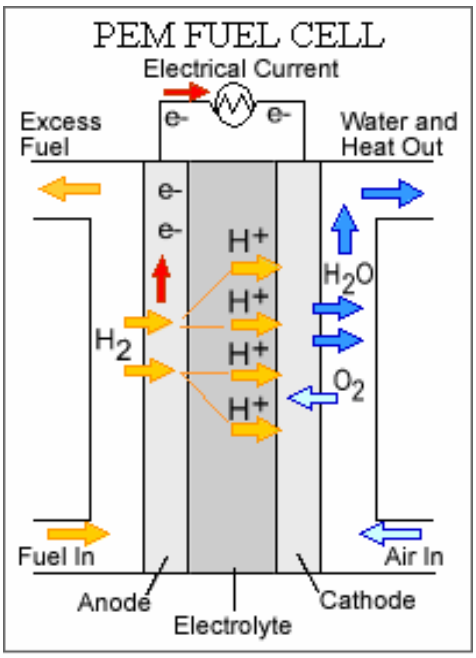

Figure 1.5: PEM Fuel Cell [17].

The following chapter will provide a general overview of metal hydrides and the complex metal hydrides investigated for this report.

CHAPTER 2

INTRODUCTION TO COMPLEX METAL HYDRIDES

2.1 General Overview

In a simple definition, metal hydrides are metallic elements (one or more metal elements) bonded with hydrogen. There are various types of metal hydrides which can be classified by the amount of different species present in the molecule: binary, ternary and quaternary hydrides (refer to Table 2.1).

Table 2.1: Classification of Metal Hydrides.

Classification	Example
Binary [18]	LiH, MgH_2, etc.
Ternary [18]	$LiBH_4$, $Zn(BH_4)_2$, etc.
Quaternary	$LaMg_2NiH_7$ [19], $LiMg_2RuH_7$ [20], etc.

The general reaction for hydrogen desorption (reaction 1) and absorption (reaction 2) for binary metal hydrides is as follows:

$$MH_n \rightarrow M + \frac{n}{2} H_{2(g)} \quad (1)$$

$$M + \frac{n}{2} H_{2(g)} \rightarrow MH_n \quad (2)$$

Ternary and Quaternary metal hydrides follow complex reactions path which are specific for each compound. Due to different molecular combination as seen in Table 2.1, metal hydrides exhibit a wide array of characteristics and properties.

Several of these materials are being investigated as possible candidates for on-board hydrogen storage. An idea on how the metal hydrides would be processed during the hydrogen economy is depicted in Figure 2.1 using sodium borohydride ($NaBH_4$).

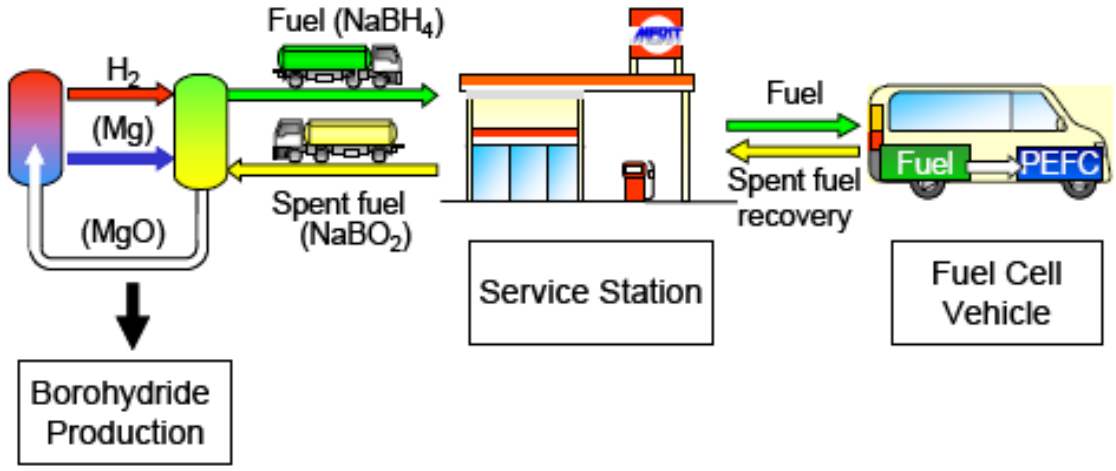

Figure 2.1: Hypothetical Hydrogen Economy Using $NaBH_4$ as Hydrogen Storage [21].

There are key general requirements that the metal hydride candidate must meet before its selection [22]:

(1) Favorable thermodynamics.

(2) Fast release and absorbing of hydrogen.

(3) High gravimetric and volumetric hydrogen capacities.

(4) Negligible change in hydrogen absorption/desorption storing capacity.

The DOE (Department of Energy) [23] and FreedomCAR Hydrogen Storage Team [24] developed specific technical targets to consider a prospective compound as a hydrogen storage system. Partial data for the year 2015 is presented in Table 2.2.

Table 2.2: DOE and FreedomCAR Hydrogen Storage Team Technical Targets [23, 24].

Technical Targets	Year 2015
Specific energy (MJ/kg)	10.8
Gravimetric capacity (kg H_2/kg system)	0.09
Volumetric Capacity (kg H_2/L system)	0.081
Energy density (MJ/liter)	9.72
System cost ($/kg system)	3
Operating temperature (^oC)	-20/50
Cycle life (cycles)	1500
Delivery pressure (bar)	2.5
Refueling rate (kg H_2/min)	2.0

Several metal hydrides and compounds satisfy some of the requirements on Table 2.2, but still lack in others. Investigations have been performed to store hydrogen in compressed tanks or as liquefied H_2 [25], however application for on-board storage is limited due to low volumetric capacity and safety issues. Recent work has been done with methane reforming as a method to produce hydrogen. Unfortunately, this process is energy intensive [26]. Metal hydrides compounds located on the upper right hand side of the graph on Figure 2.2 are considered the best materials for hydrogen storage applications [27]. Sodium aluminum hydride shows promise of filling the hydrogen storage technical needs however, several investigations indicates a low hydrogen release at high temperatures and poor cyclic reversibility due to partial reactions [28 – 32]. For our research, doped and undoped mixtures of $LiBH_4$ and MgH_2 and additional ones ($Zn(BH_4)_2$ and dopants) were investigated. The following sections will continue briefing about the background of the compounds and its different properties.

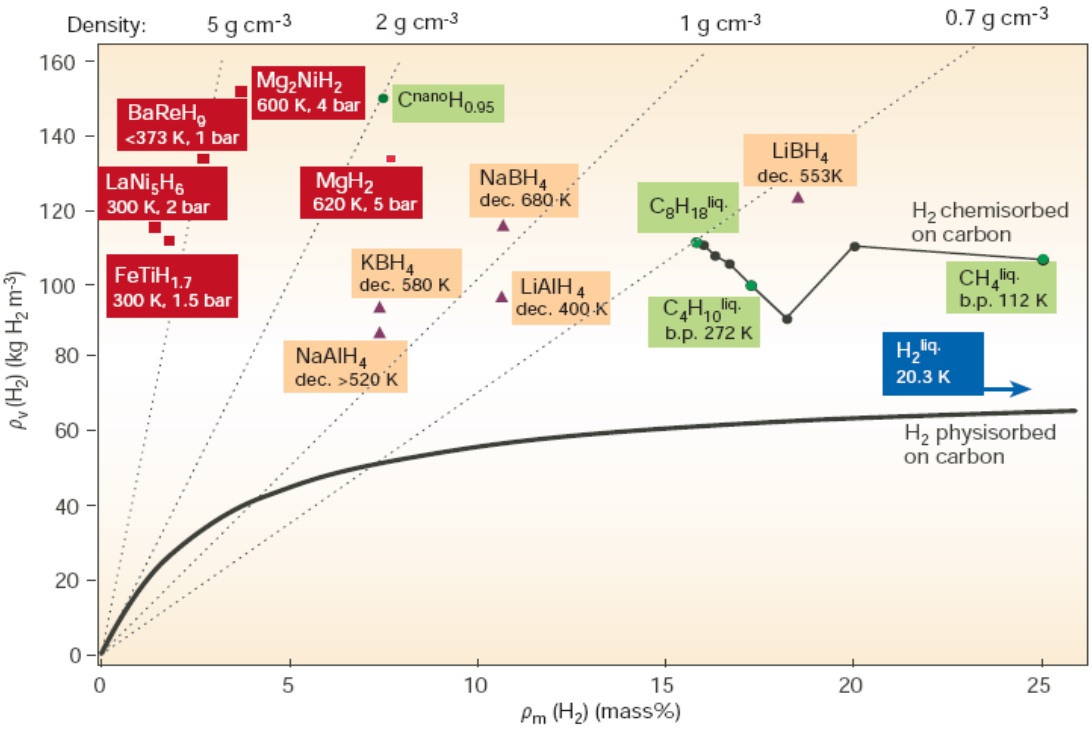

Figure 2.2: Comparison of Volumetric and Gravimetric Hydrogen Capacities for Some Metal Hydrides [16].

2.2 Lithium Borohydride ($LiBH_4$)

$LiBH_4$ is one of the light weights and high hydrogen storage capacity material. It has a theoretical gravimetric and volumetric hydrogen storage capacities of 18.5 wt.% and 121 kgH_2/m^3, which surpasses the DOE and FreedomCAR targets (refer to Table 2.2). Initial investigations have demonstrated that the hydrolysis reaction (3) [33-35] of lithium borohydride at room temperatures effectively releases hydrogen exothermically; however the process is irreversible with $LiBO_2$ as byproduct. Hydrolysis reaction proceeds as follows:

$$LiBH_4 + 2H_2O \rightarrow LiBO_2 + 4H_2 \qquad (3)$$

An alternate route that has been previously investigated is to thermally destabilize $LiBH_4$. Lithium borohydride has a known melting point around 275°C [36] with the following thermal properties investigated by Fedneva et al. [37], refer to Table 2.3:

Table 2.3: Thermal Analysis of Lithium Borohydride According to Fedneva et al. [37].

Temperature Range (°C)	Description
108–112	Endothermic peak. Structural transition.
268–286	Fusion process with a slight weight loss.
380	Main weight loss due to H_2 decomposition.
483–492	Authors are not certain however, it coincides with a weight loss.

Recent thermal studies by Zuttel et al. [38, 39] and Orimo et al. [40] further expands the understanding regarding lithium borohydride behavior (see Table 2.4 and 2.5).

Table 2.4: Thermal Studies by Zuttel et al. on Lithium Borohydride [38, 39].

Temperature Range (°C)	Description
100	Structural transition with a slight weight loss.
270	Fusion phase.
320	First significant weight loss.
400–500	Second significant weight loss.

Table 2.5: Thermal Studies by Orimo et al. on Lithium Borohydride [40].

Temperature Range (K)	Description
380 (~107°C)	Structural transition.
550 (~277°C)	Melting phase.
600–700 (~327–427°C)	Dehydriding reaction.

As an additional note, the structural transition of lithium borohydride has been found to be from orthorhombic [41] to hexagonal structure [42-44].

According to Stasinevich and Egorenko [45], the decomposition of alkali metal tetrahydroborides can proceed as reactions (4) or (5):

$$MBH_4 \rightarrow M + B + 2H_2 \quad (4)$$

$$MBH_4 \rightarrow MH + B + \frac{3}{2}H_2 \quad (5)$$

For lithium borohydride, the dehydriding reaction (6) [38] and rehydriding reaction (7) [40] can be generally described as:

$$LiBH_4 \rightarrow LiH + B + \frac{3}{2}H_2 \quad (6)$$

$$LiH + B + \frac{3}{2}H_2 \rightarrow LiBH_4 \quad (7)$$

Theoretically the reaction (6) releases around 13.8wt% of hydrogen. According to Orimo et. al [40], the rehydrogenation of lithium borohydride was achieved however, the energy levels consumed during this process, 35Mpa of hydrogen and 873K, might not make it cost effective. Additional investigations performed with lithium borohydride, included the doping with SiO_2 as a catalyst thus enabling the decrease of $LiBH_4$ dehydriding temperature to 300^{o}C [39]. A recent report indicates a dehydrogenation-rehydrogenation cycle improvement and reducing the reaction enthalpy of $LiBH_4$ by the addition of MgH_2 in a ratio of $2LiBH_4 + MgH_2$ [46]. The addition of MgH_2 reversibly destabilizes $LiBH_4$ which in consequence increases the hydrogen equilibrium pressure as reaction (8) [46]:

$$LiBH_4 + \frac{1}{2} MgH_2 \leftrightarrow LiH + \frac{1}{2} MgB_2 + 2H_2 \quad (8)$$

Part of the investigation was dedicated to further understand the behavior of $2LiBH_2 + MgH_2$. The report will discuss the significant results obtained while studying the system. The next section will briefly introduce the compound used during the research MgH_2.

2.3 Magnesium Hydride (MgH_2)

Magnesium hydride is a non-expensive binary hydride with a theoretical hydrogen capacity around 7.6wt% [18]. It can effectively store hydrogen due to its thermodynamic stability however reaction kinetics are too slow and the decomposition temperature is high, approximately at 330^{o}C [18].

Different approaches to improve the reaction kinetics of MgH_2 have been taken, including the mechanical milling. The mechanical milling of a hydrogen absorbing compound, in this case MgH_2, under hydrogen pressure leads to hydrogen uptake, defects and changes in the surface [47-50] however the attention is more focused on the effective reduction of the desorption temperature by ball milling [51-55]. Experiments have taken place in order to catalytically improve MgH_2 kinetics with Nb_2O_5 [56, 57]. More studies involve the addition of small amounts of Ti, V, Mn, Fe, Ni mechanically milled with MgH_2 reporting good results [58-62]. A recent approach is the use of magnesium nickel alloys for hydrogen storage systems [63-65], the presence of nickel improves the hydriding and dehydriding rates. The MgH_2/nanoNickel system was investigated and the results presented in this report discussing the effects of nanoNickel. In addition, mixture

of the system with dopants was also compared with Vajo's et al. [46] in this document and will be discussed in Chapter 4. The next session will briefly introduce a studied compound $Zn(BH_4)_2$.

2.4 Zinc Borohydride ($Zn(BH_4)_2$)

$Zn(BH_4)_2$ is a ternary complex metal borohydride with a decomposition temperature of around 85°C [18]. Its theoretical hydrogen capacity is about 8.5wt% and it can be synthesized by metathesis reaction of $NaBH_4$ and $ZnCl_2$ in diethyl ether [66]. A recent report from Eun Jeon et al. [67] indicates that zinc borohydride was successfully synthesized by ball milling zinc chloride and sodium borohydride without the use of a solvent, see reaction (9):

$$ZnCl_2 + 2NaBH_4 \rightarrow Zn(BH_4)_2 + 2NaCl \qquad (9)$$

For this report, the possible formation of $Zn(BH_4)_2$ by ball milling $LiBH_4$ and $ZnCl_2$ would be explained, however additional investigations are needed to determine its presence.

CHAPTER 3

MATERIALS, EQUIPMENTS AND APPROACH

3.1 Experimental Materials

Table 3.1 provides a list of the materials used during the investigation. These materials are used without further purification except drying inside the N_2/vacuum glove box for O_2 and moisture removal.

Table 3.1: List of Materials.

Name of material	Purity	Manufacturer
$ZnCl_2$	99.999%	Sigma-Aldrich
$TiCl_3$	99.999%	Sigma-Aldrich
$LiBH_4$	95%	Alfa Aesar
TiF_3	99.999%	Sigma-Aldrich
nanoNi	99.99%	QuantumSphere
nanoNi	99.9%	Sigma-Aldrich
nanoZn	99+%	Sigma-Aldrich
MgH_2	98%	Alfa Aesar
Polyethylene foil (thin foil)	unknown	Target Brands, Inc.

3.2 General Approach

The general procedure followed for the investigation is represented in Figure 3.1.

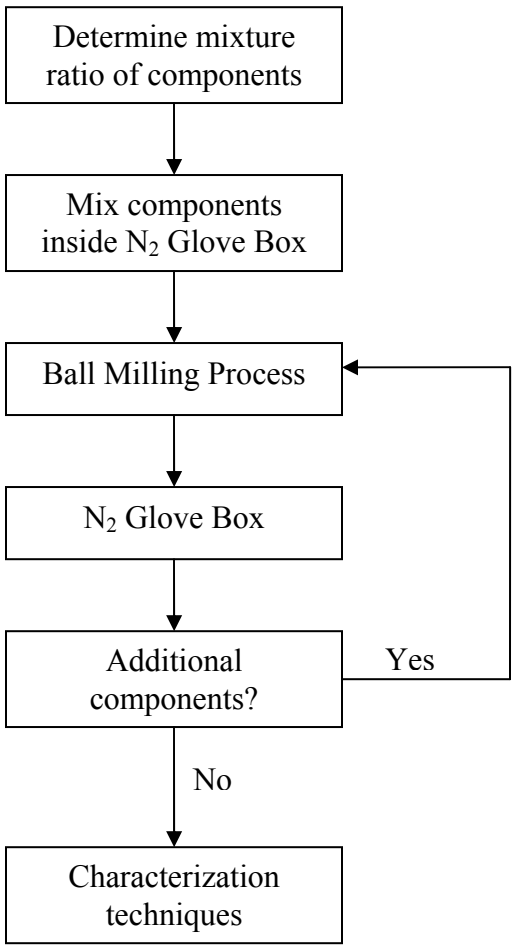

Figure 3.1: Procedure Followed During the Investigation.

The approach specified in Figure 3.1 would have a general formula to distinguish if the mixture has not been altered with additional components. The formulas would be shown in the plot legend as follows:

$$A + B + C + BM\ \ time \tag{10}$$

$$A + B + C\ \ BM\ \ time \tag{11}$$

Formulas (10) and (11) indicates that components A, B and C were first mixed together and then ball milled (BM in the formula is an abbreviation for ball milling) for a certain amount of time. However, if an additional component was added to the mixture and then ball milled again. The formulas would be presented in the plot legend as follows:

$$(A + B + C + BM\ \ time) + D + BM\ \ time \quad (12)$$

$$(A + B + C + BM\ \ time) + D\ BM\ \ time \quad (13)$$

Formulas (12) and (13) indicates that components A, B and C were first mixed together and then ball milled (BM in the formula is an abbreviation for ball milling) for a certain amount of time, however an additional component D was added afterwards and then ball milled again. As an example, if the plot legend states: MgH_2 BM9hrs + 10mol% nanoZn + BM2hrs. It indicates that MgH_2 was previously ball milled for 9 hours then mixed with 10 mol% of nano-Zinc and the new mixture ball milled for 2 hours. This method would enable the readers to understand the legend on each plot still, to avoid confusion, a full explanation as detailed before will be provided.

3.3 General Procedure

All mixing, transfer and weighing was carried out in a nitrogen filled glove box to reduce the contact of oxygen and moisture with the samples. The mixtures were mechanically milled in a high energy Fritsch pulverisette planetary mono mill P6 using a stainless steel bowl (80 ml and 250ml) sealed with a specially designed lid with two Schrader valves on opposite corners and a viton O-ring (refer to Figure 3.2).

Figure 3.2: Ball Milling Bowl and the Specially Designed Lid with Schrader Valves.

A ball to powder weight ratio of 20:1 and a milling speed of 300 rpm were set to optimize the process over a varied range of milling times. Several milling durations were employed during the investigation ranging from 20 minutes to 2 hours. The ball milling time and procedure will be further discussed in details for each result in Chapter 4. Hydrogen flushing/purging was performed prior ball milling to every mixture in order to reduce the presence of oxygen and/or moisture inside the bowl during the process. For ball milling times below 30 minutes the system was purged only once at the beginning, before starting the process however; for milling times higher than 30 minutes (i.e. 1 hour) the purging was performed every 30 minutes. After ball milling, the as-prepared mixture of complex hydrides were immediately transferred to the glove box for further characterization analysis.

Weight loss analyses were performed using a SDT-Q600 instrument from TA Instruments. For SDT-Q600 measurements the samples were loaded in alumina pans and set the general temperature ramp rate at around 5^{o}C/min. All calibrations were performed

as per TA instruction manual. The Universal Analysis software V4.0C was employed to analyze the results obtained from both equipments. An additional note, the to-be-measure samples were handled inside the nitrogen filled glove box at all times except when purging with hydrogen.

The measurement for isothermal volumetric sorption was carried out by a Hy-Energy's PCT Sievert's type apparatus. Volume calibration was performed with and without the sample until a constant temperature with accuracy of ±1° C was achieved. A Lab View software program was employed for data monitoring and recording. The measurement analyses were performed using Hy-Analysis macros in the Igor program.

The powder X-ray diffraction (XRD) analyses were carried out using a Philips X'pert diffractometer with CuKα radiation of λ= 5.4060 Å. As part of the Incident Beam Optics, a Fixed Divergence slit module was used along with a 1^{o} Fixed slit, a 10mm Beam mask and Soller slit of 0.04 rad. The accessories used for the Diffracted Beam Optics were: a Programmable Receiving Slit with fixed anti scatter slit, a 2^{o} anti scatter slit, a monochromator and detector. The collected XRD patterns were analyzed employing the software PANalytical X'pert Highscore software version 1.0e for phase identification and crystalline size. A polyethylene clear plastic wrap (thin foil) was used to protect the samples from air and moisture by wrapping the sample holder completely with the thin foil (see Figure 3.3). The thin foil shows diffraction peaks in the 2θ range of 21–28º.

Figure 3.3: XRD Sample Holder Covered with Polyethylene Clear Plastic Wrap.

The Perkin-Elmer *one* FT-IR spectrometer was used in order to study the B-H bonds or other possible chemical bonds in the $2LiBH_4$ / MgH_2 mixtures, which would be discussed in Section 4.3.

3.4 Equipments

3.4.1 Nitrogen Filled Glove Box

As a general definition, the glove box is a sealed container designed to maintain special atmospheric conditions while also allowing the investigator to manipulate the objects or objects placed inside of it. The principal components of the glove box are (refer to Figure 3.4 and 3.5):

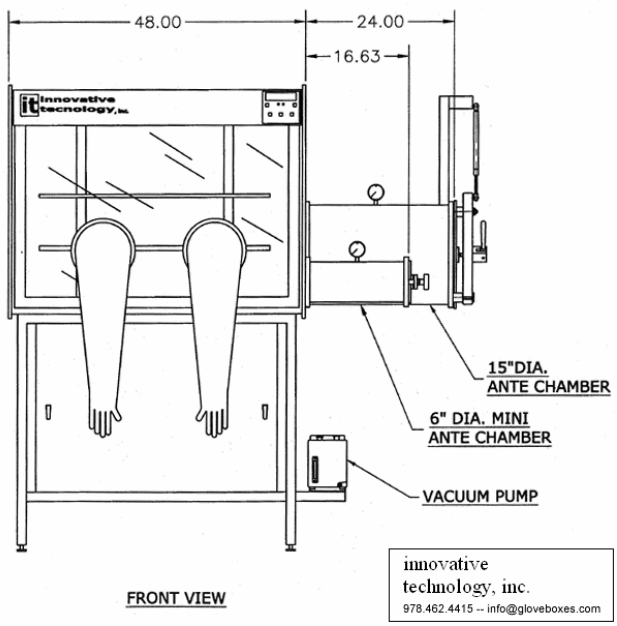

Figure 3.4: TA Instruments Diagram of Glove Box [68].

(1) Gloves.

(2) Vacuum pump.

(3) Electronic sensors to monitor oxygen and moisture content.

(4) Two antechambers or ports used to transfer materials in and out of the glove box; both ports can be opened from the inside and outside the box.

(5) The automatic gauge controls maintains the pressure inside the glove box, the system will increase or reduce pressure by injecting nitrogen or evacuating with vacuum pump, respectively according to the pressure range set for operation.

(6) The foot pedal, it allows the investigator to manually adjust the pressure inside the glove box.

(7) The purification system removes and maintains low levels (less than 1ppm) of oxygen and moisture inside the gloves by continuously reprocessing (refer to Figure 3.6) the nitrogen through a molecular sieve of (Al_2O_3) alumina and copper catalyst.

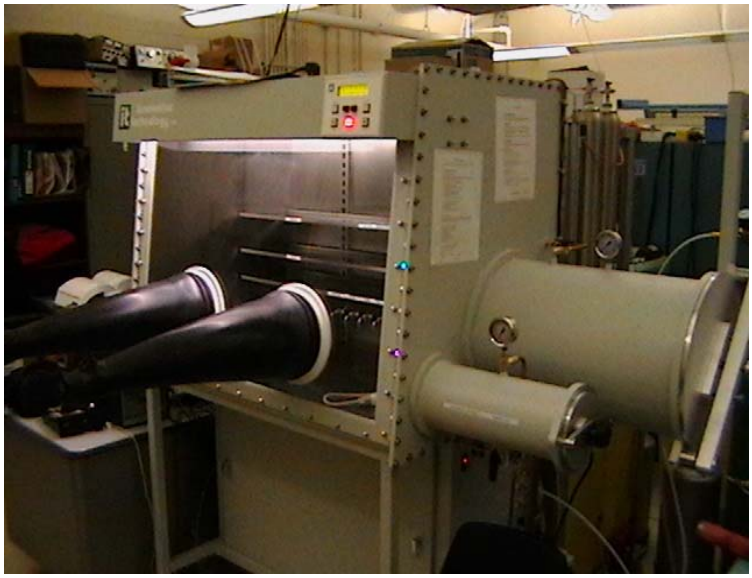

Figure 3.5: Picture of Glove Box.

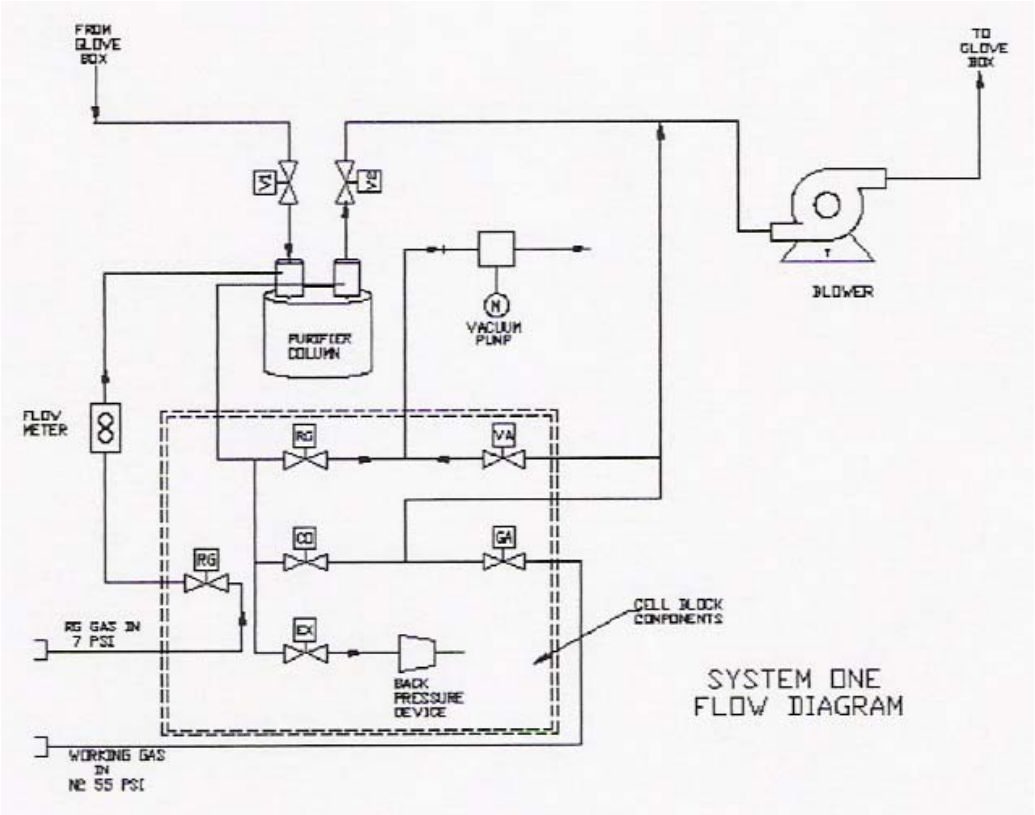

Figure 3.6: Glove Box System Flow Diagram [69].

3.4.2 Ball Mill (BM)

A high energy Fritsch pulverisette planetary mono mill P6 (see Figure 3.7) was used for mixing and synthesis of complex metal hydrides.

Figure 3.7: Picture of Ball Mill Equipment [70].

Other processes can be achieved using the ball milling such as: particle size reduction and structural alterations of particles. The ball milling operation is as follows: the bowl is placed on the grinding platform (note: the platform has a counter weight to minimize vibrations due to imbalances), secured to the platform with the safety features and programmed to rotate either clockwise or counter clockwise. The grinding bowl's rotational movement is opposite of the supporting disk movement (refer to Figure 3.8). The centrifugal force (up to 10 g's acceleration) provides energy and motion to the grinding balls which are rolled halfway around the bowl and then, due to centrifugal force, thrown across the bowl to impact the sample on the opposite side at high speed.

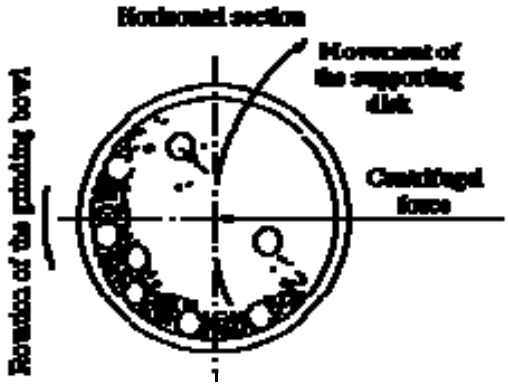

Figure 3.8: Cross-Sectional Diagram of the Planetary Ball Mill Movement [71].

3.4.3 Simultaneous DSC and TGA – (SDT)

The SDT measures heat flow (enthalpic changes) and weight changes related with transitions and reactions in materials. The equipment has the capability to assist in the differentiation of endothermic and exothermic processes with no weight loss (e.g., melting and crystallization) from those with weight changes (e.g., desorption). The operational temperature range for the model (SDT-Q600) ranges over the ambient to 1500^{o}C. The furnace is a one piece alumina sample tube surrounded by a platinum rhodium heater (refer to Figure 3.9) which can be set with heating rates of up to 100^{o}C/min and 25^{o}C/min for final temperatures of 1000^{o}C and 1500^{o}C, respectively. The balance beams are made of ceramic alumina with platinum liners platform at the furnace end. Platinum/Platinum-Rhodium thermocouples inside the ceramic beams from the platform to the meter mount provide the thermal measurements (refer to Figure 3.10). To prevent back-diffusion from the samples and contamination to the balance housing, the area is carefully purged with inert gas (in this case N_2) (refer to Figure 3.11). The SDT-

Q600 was enclosed inside a glove box to reduce samples exposure to air (refer to Figures 3.12 and 3.13).

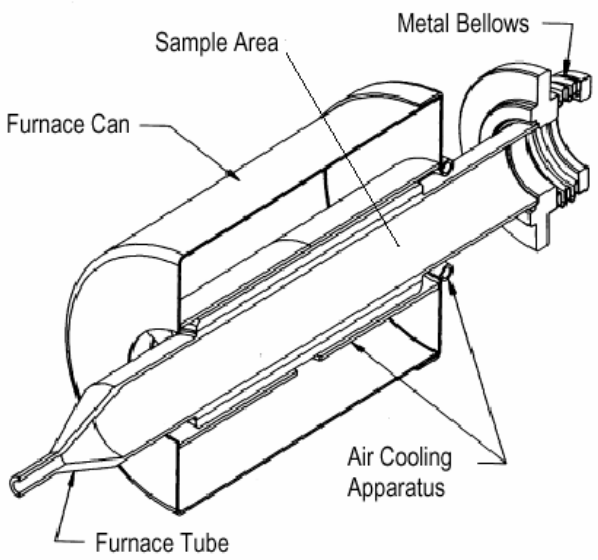

Figure 3.9: Cross-Sectional Diagram of SDT Furnace [72].

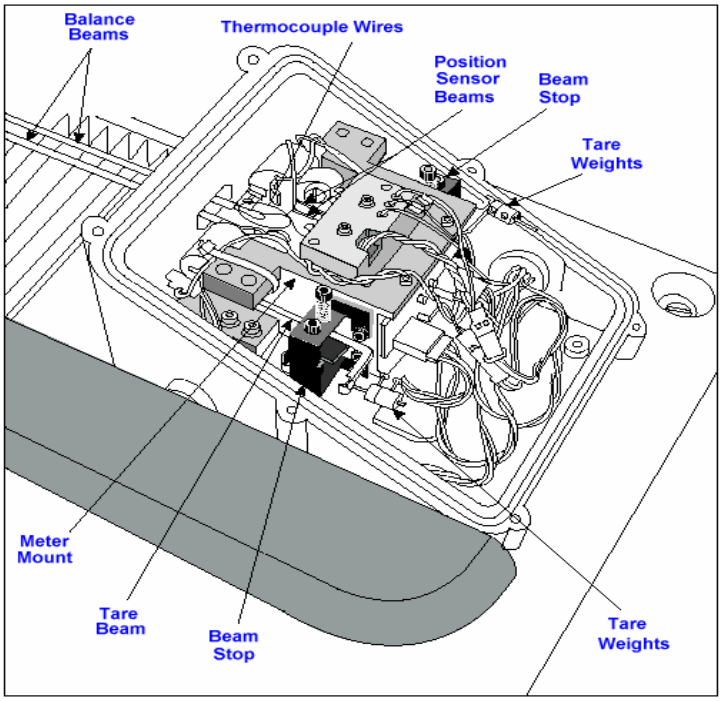

Figure 3.10: SDT Balance Housing [72].

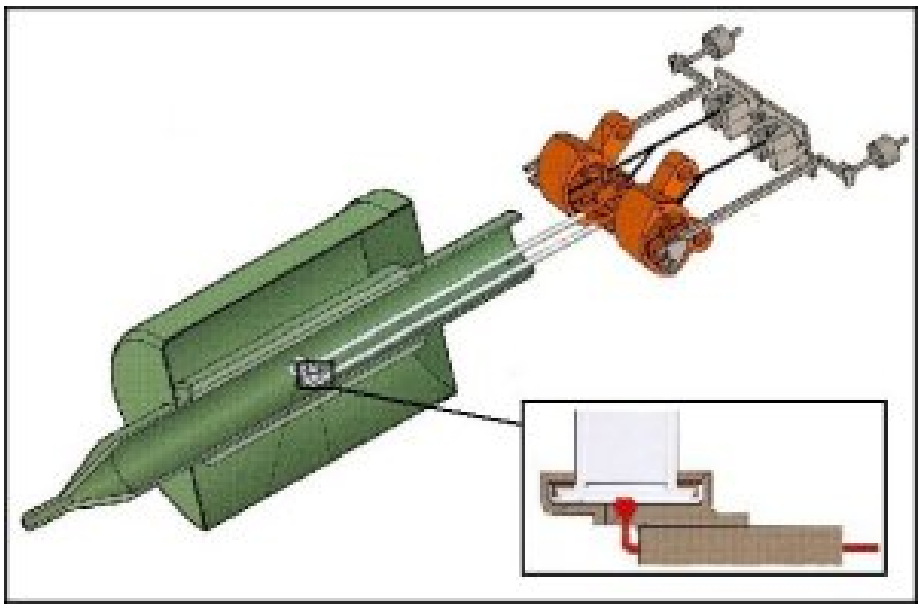

Figure 3.11: Full Cross-Sectional Diagram of SDT-Q600 [73].

The TGA portion of the instrument operates as follows; the balance arms (ceramic beams) are maintained in a horizontal null position while a position sensor sends an equal amount of light (supplied by a constant current infrared LED) to each of the photodiodes. If weight is lost or gained, the beam positions shifts causing an unequal amount of light to strike the photodiodes. The unequal amount of light is then transferred as a change in current which is proportional to the weight change.

The DSC portion employs a single heat source (Platinum Rhodium heater) and two symmetrically located and identical sample platforms (ceramic beams) with thermocouples inside and along the beams length. The platforms symmetry is necessary in order to uniformly apply heat. The analysis works converting the heat flow to the thermal equivalent of Ohm's Law.

Figure 3.12: SDT-Q600 Photo.

Figure 3.13: SDT-Q600 Inside an Inert Atmosphere Glove Box.

3.4.4 X-Ray Diffractometer (XRD)

X-ray Powder Diffraction (XRD) is a technique which employs collimated monochromatic x-rays for characterization and identification of crystalline structure. Additional uses include: qualitative and quantitative phase identification, identification of lattice parameters, thin film studies, etc. A Philips X'pert diffractometer with CuKα radiation of λ= 5.4060 Å, was employed for such purposes during the investigation. The cathode emits and accelerates the electrons into the vacuum by high voltage while the anode collects them establishing a current flow. The electrons impact the metal target (in this case copper) and produce X-rays, which are incident on the sample. The diffraction takes place when X-rays are diffracted by their interaction with the atomic plane arrangement in the crystal.

The basic principle of Bragg-Brentano geometry was used for the powder diffraction. According to Bragg's Law, when X-rays are scattered from a crystal lattice constructively, not destructively (refer to Figure 3.14 and 3.15), peaks of scattered intensity are observed that satisfies the Bragg equation (13) given below:

$$n\lambda = 2d\sin(\theta) \tag{13}$$

Where θ is the angular position between the incident and diffracted rays, d is the spacing between the planes of atoms lattice, n is an integer, λ is the wavelength of x-rays. A picture of the XRD equipment used as a characterization tool is provided in Figure 3.16.

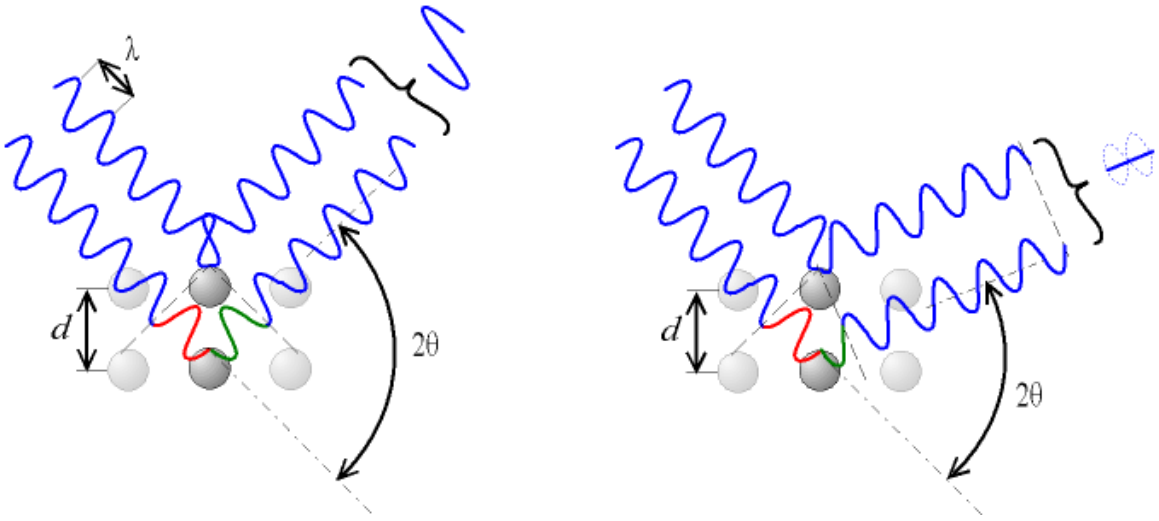

Figure 3.14: Constructive (Left Picture) or Destructive (Right Picture) Interferences [74].

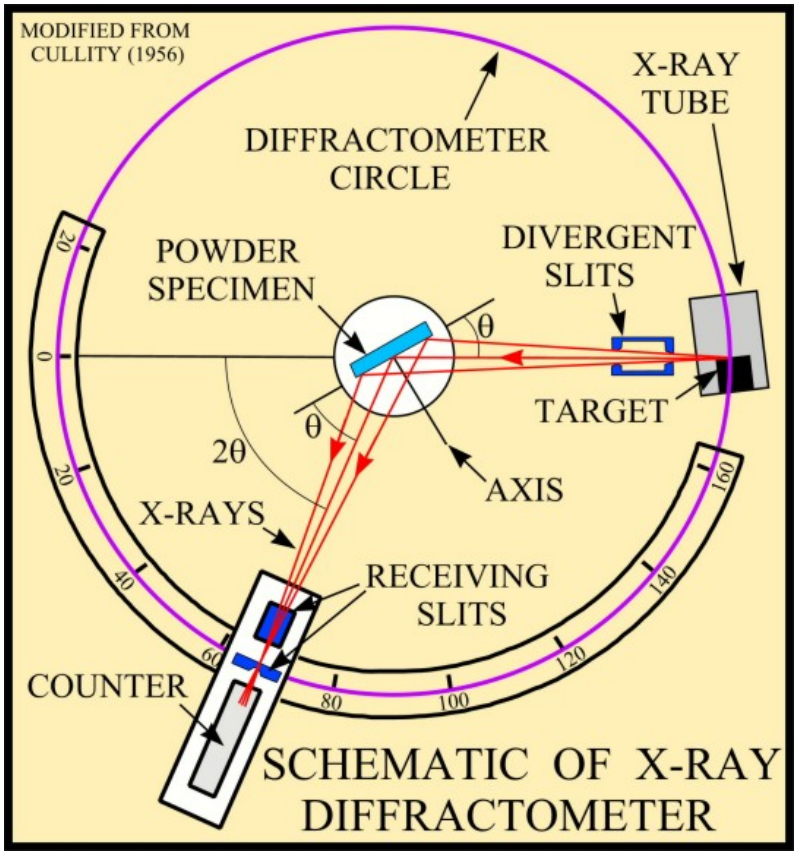

Figure 3.15: Schematic of an X-ray Diffractometer [75].

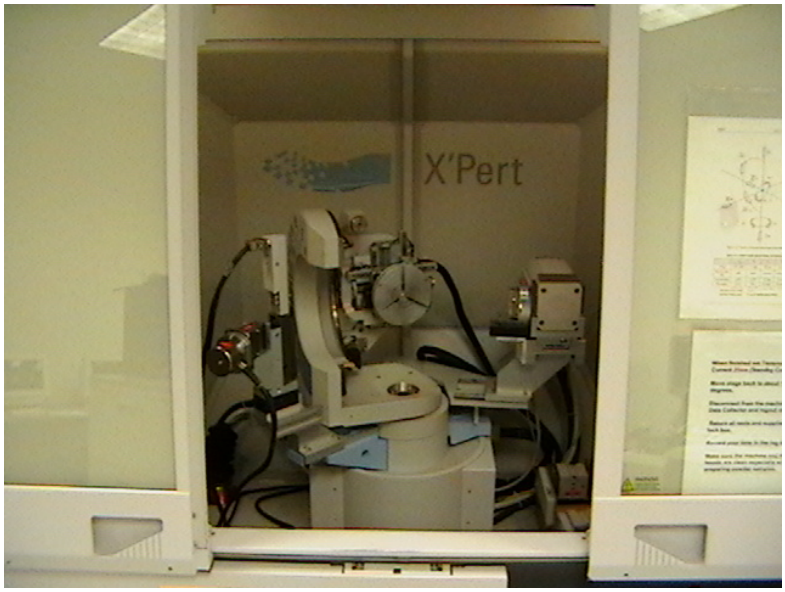

Figure 3.16: X'pert Diffractometer Picture.

3.4.5 Pressure Composition Isotherms (PCI) Apparatus

The PCI or PCT is an automated Sieverts type apparatus use to measure gas sorption properties of materials, in this case hydrogen sorption in metal hydrides. The model use during the investigation was the PCTPro-2000 by Hy-Energy LLC., USA. The model offers several features for measurements such as: PCI (Pressure Composition Isotherms), Gas Sorption Kinetics, Heat of Formation, Cycle-Life Kinetics, Cycle-Life PCT, Volume Calibration and Packing Density measurements [76]. There are important preparation processes, where no data is collected, that must be performed prior the experiments in order to prevent leaks, contamination, damage, etc.:

(1) Purge Gas Lines – when a new gas or bottle has been connected.

(2) Purge System & Samples – when a connection with a possible contaminant gas has been made.

(3) Leak Check – for every experiment.

As a general basic PCT operation, the reactor with the sample is connected and a leak check is performed using Helium (99.9999% pure). Afterwards, the reactor volume is calibrated at constant temperature and to a set measured pressure. Hydrogen absorption is calculated by measuring the pressure difference. Arrhenius plots can be obtain using the kinetic feature option by increasing the temperature in intervals to obtain Log (sorption rate) vs. 1000/temperature. In addition, van't Hoff plot represents the thermodynamic equilibrium of the gas sorption process. The PCT feature is used to obtain the van't Hoff measurements. The enthalpy of formation, which is represented by the slope in the van't Hoff plot, can be calculated by the van't Hoff equation:

$$\ln(P_{eq}) = \frac{\Delta H}{R}\left(\frac{1}{T}\right) - \frac{\Delta S}{R} \qquad (14)$$

The temperature is held constant while gas (pressure) is applied to the sample in aliquots, for each aliquot the system is allowed to reach equilibrium. The process can be repeated until desired or until operational limits allows. If hydrogen is absorbed or desorbed by the sample, a plateau forms (see Figure 3.17) indicating hydrogen-sample interaction at that specific temperature and pressure. A picture of the model and monitor indicator can be observed in Figure 3.18 and 3.19.

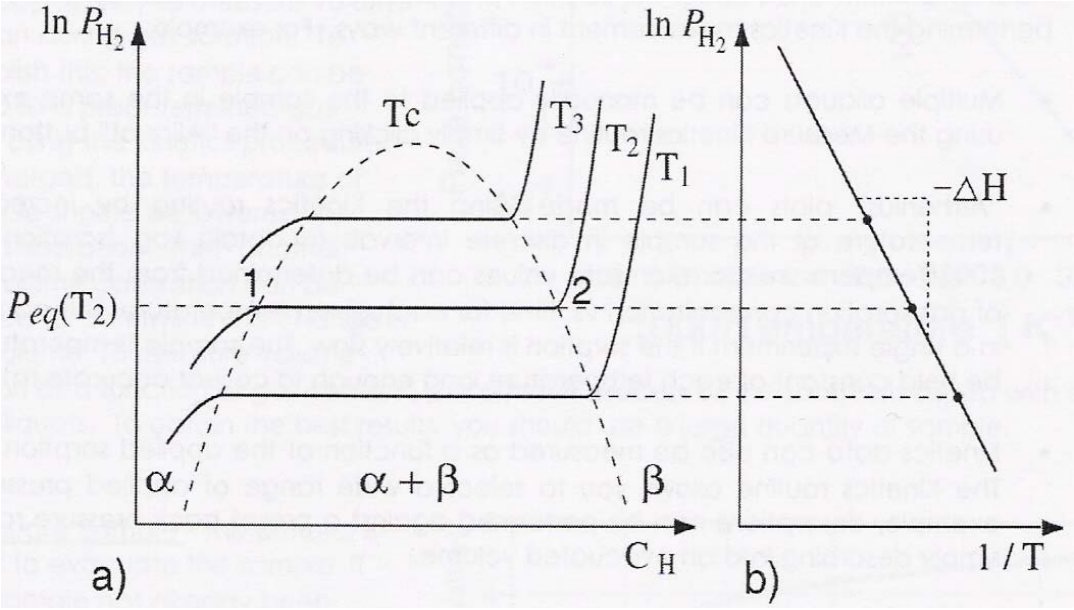

Figure 3.17: PCT Diagram (Left) Associated with the Van't Hoff Plot (Right) [76].

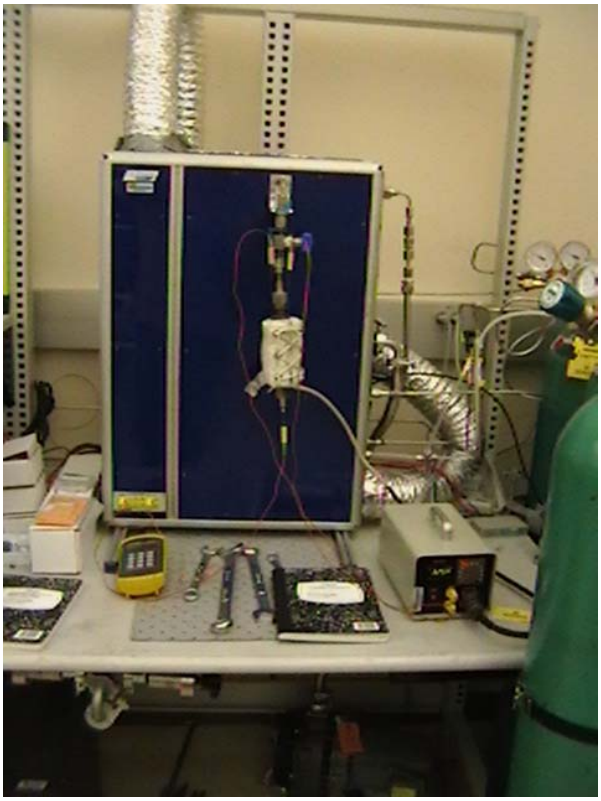

Figure 3.18: PCTPro-2000 Hydrogen Sorption Apparatus Picture.

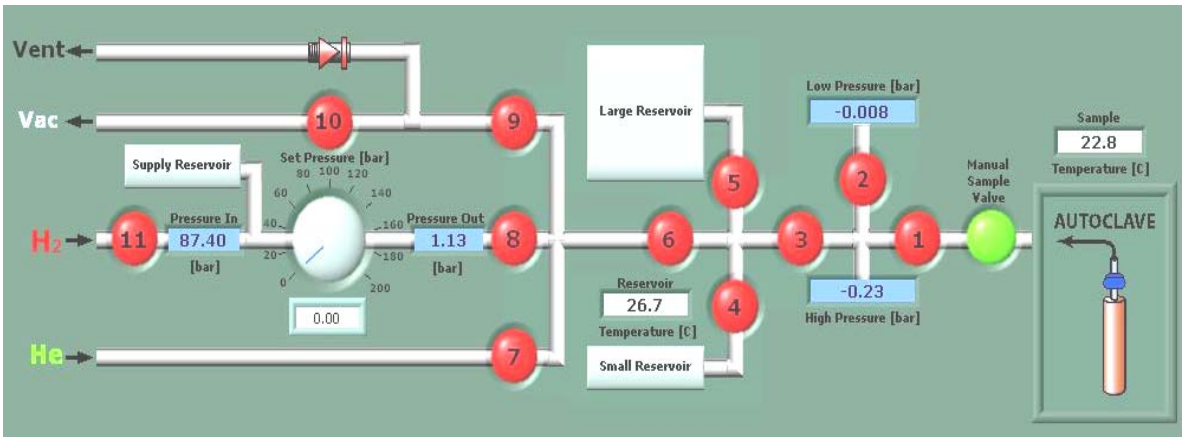

Figure 3.19: PCTPro-2000 Manifold Monitor Indicator.

3.4.6 Fourier Transform Infrared Spectrometer (FT-IR)

Fourier Transform Infrared (FT-IR) spectroscopy is an analytical technique used to measure infrared intensity against wavelength of light. However, multiple regions are found in the infrared portion of the electromagnetic spectrum which is divided into three; the near- (14000-4000 cm^{-1}), mid- (approx. 4000-400 cm^{-1}) and far- infrared (approx. 400-10 cm^{-1}) named for their relation to the visible spectrum. The Infrared spectroscopy is useful because chemical bonds interact with the matter by stretching, contracting and bending the chemical bonds at different energy levels. The far-infrared, has low energy and could be used for studies of rotational spectroscopy, the mid- infrared for associated rotational-vibrational structure and near- infrared for harmonic vibrations.

In order to measure a sample, a beam of infrared light is passed through an interferometer creating constructive and destructive patterns of light beams which are then passed through the sample. By absorbing an amount of energy at each wavelength, a spectrum is created and recorded. From this transmittance or absorbance spectrum may

be plotted showing at which wavelengths the sample absorbs the IR and as consequence, the chemicals bonds present.

A Fourier transform spectrometer is a Michelson interferometer with a movable mirror. In its simplest form, a Fourier transform spectrometer might look like Figure 3.20.

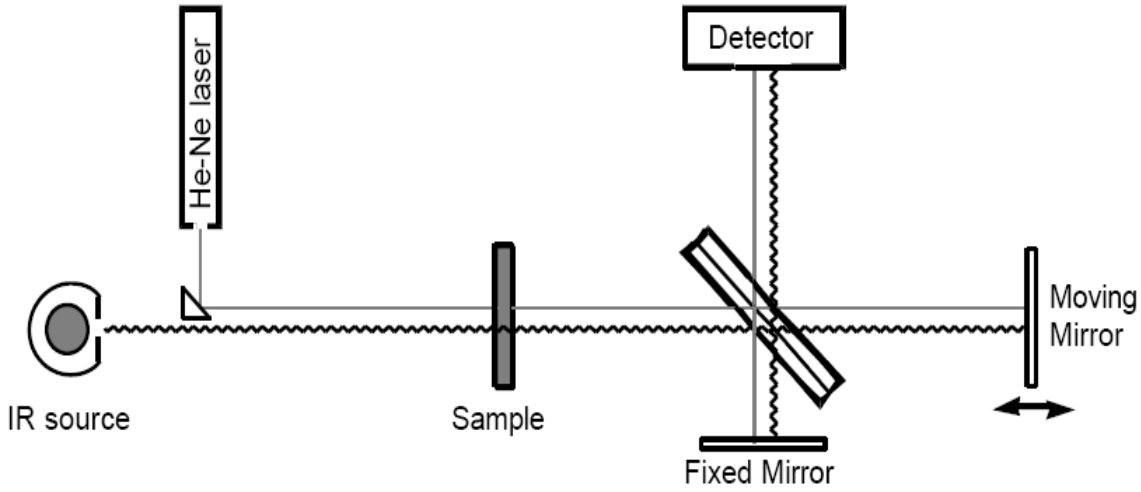

Figure 3.20: Basic Diagram for an FT-IR Spectrometer [77].

CHAPTER 4

RESULTS AND DISCUSSION

4.1 Undoped and Doped $LiBH_4 + ZnCl_2$

Figures 4.1 and 4.2 show the different thermal and weight loss profiles for undoped and doped (with MgH_2, TiF_3 and nanoNi) $2LiBH_4 + ZnCl_2$, including an undoped 10 minutes hand mixed sample. The mixture of $LiBH_4$ / $ZnCl_2$ in a ratio of 2:1, was prepared by ball milling under hydrogen pressure. As a clarifying point to the reader, all $LiBH_4$ / $ZnCl_2$ mixtures, with the exception of the 10 minute hand mixed sample, were ball milled for 20 minutes. The profiles indicates the presence of a complex metal hydride, probably $Zn(BH_4)_2$ [67]. Zinc borohydride $Zn(BH_4)_2$ has a theoretical hydrogen capacity of 8.5wt% and decomposition temperature around 100^0C. It could be formed by ball milled mixture of $2LiBH_4 + ZnCl_2$ however, further characterization is needed.

Comparing both profiles in Figures 4.1 and 4.2, the samples of $2LiBH_4 + ZnCl_2$ doped with nanoNickel (QuantumSphere) showed better kinetics and thermodynamic effects at lower temperatures when compared to the undoped sample. The catalytic effectiveness of the mixture doped with 3mol% nanoNickel surpasses the other doped and undoped mixtures by reducing the desorption temperature from 114^0C to 100^oC. The measured weight loss for most mixtures, except the hand mixed sample, is much higher

than the expected 8.5wt%, indicating a probable decomposition of additional compounds besides of hydrogen. Gas analyses should be performed to determine gas composition. No significant effects were observed for TiF_3 and MgH_2 doped samples.

A hand mixed sample was prepared using a ceramic mortar and stirring for 10 minutes; the SDT-TGA plot shows a weight loss of at least 9.0wt% at around 125^0C. The small weight loss compared to other graphs might be due to an incomplete reaction of $2LiBH_4 + ZnCl_2$. The SDT-DSC diagram indicates the presence of two endothermic peaks with onset at around 112^0C and 137^0C which could be associated with the remaining $LiBH_4$ structural transition and decomposition of $Zn(BH_4)_2$, corroborating the incompleteness of the hand milled reaction. Table 4.1 represents the SDT-TGA analysis results for the undoped and doped $2LiBH_4 + ZnCl_2$.

Table 4.1: Thermogravimetric Analysis of Undoped and Doped $2LiBH_4 + ZnCl_2$.

Sample Name	On-set Temperature (ºC)	Peak Temperature (ºC)	Total weight loss (%)
$2LiBH_4 + ZnCl_2$	114.07	125.06	14.80
$2LiBH_4 + ZnCl_2$ + 1mol% TiF_3	114.13	129.21	14.92
$2LiBH_4 + ZnCl_2$ + 2mol% TiF_3	112.57	128.00	14.18
$2LiBH_4 + ZnCl_2$ + 2mol% MgH_2	113.96	128.11	13.70
$2LiBH_4 + ZnCl_2$ Handmilled	138.69	150.50	9.435
$2LiBH_4 + ZnCl_2$ + 2mol% nanoNi	110.38	113.00	14.73
$2LiBH_4 + ZnCl_2$ + 1mol% nanoNi	114.38	116.90	13.54
$2LiBH_4 + ZnCl_2$ + 3mol% nanoNi	106.05	107.30	14.82
$2LiBH_4 + ZnCl_2$ + 4mol% nanoNi	106.65	109.31	12.67

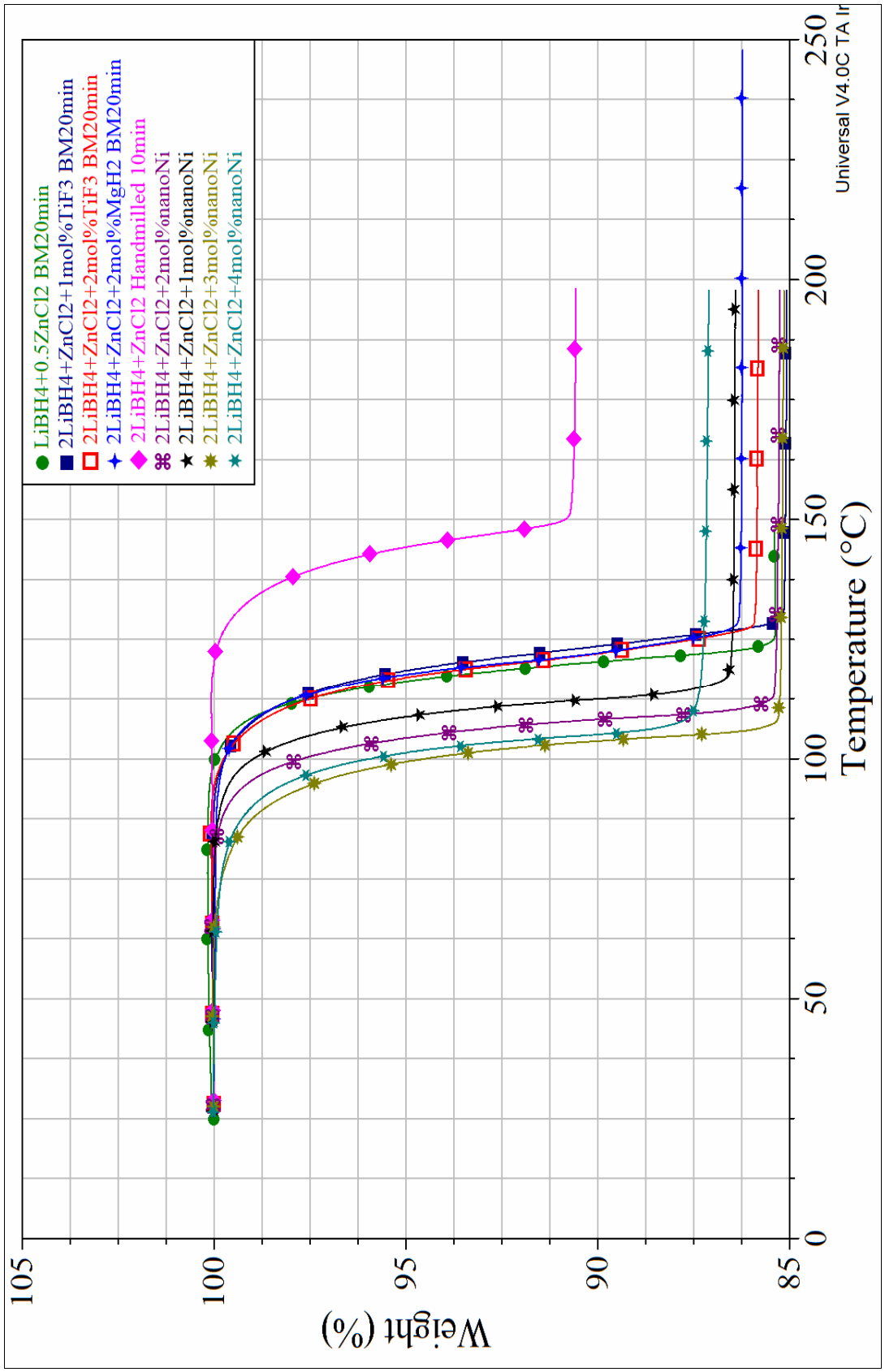

Figure 4.1: SDT-Q600 – TGA Profiles for Doped and Undoped $LiBH_4$ + $ZnCl_2$.

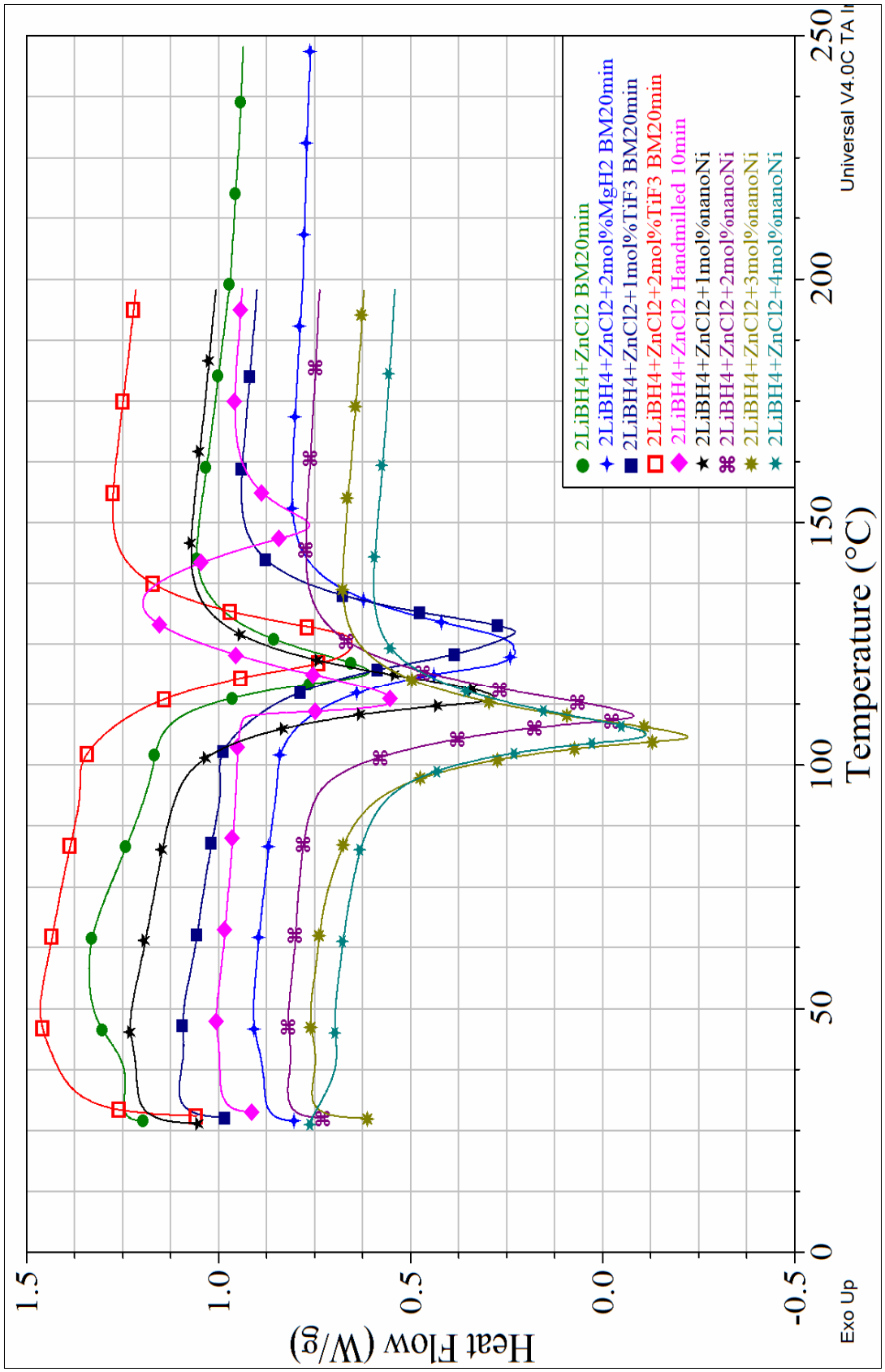

Figure 4.2: SDT-Q600 – DSC Profiles for Doped and Undoped $LiBH_4$ + $ZnCl_2$.

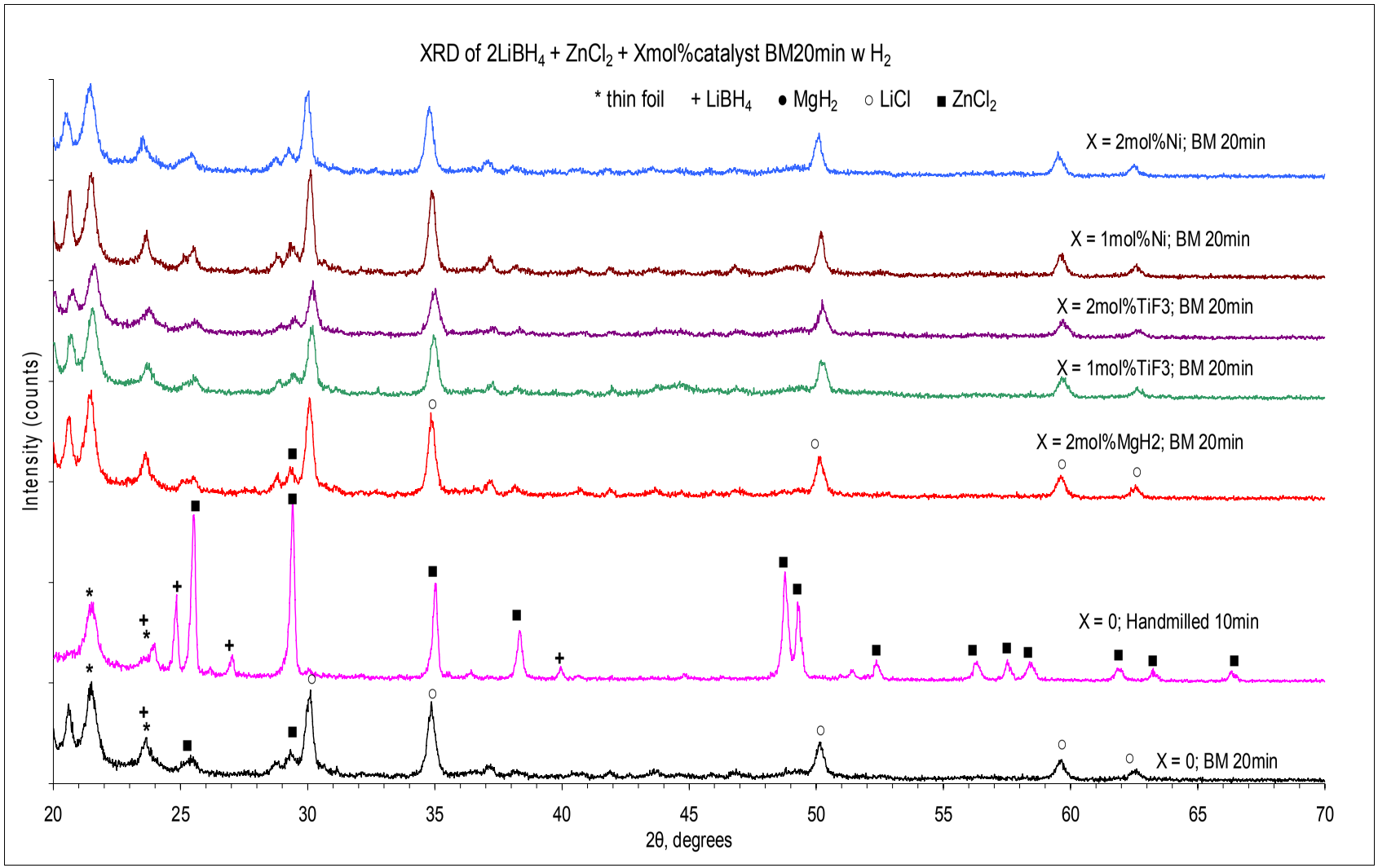

Figure 4.3: XRD Profiles for Doped and Undoped $2LiBH_4 + ZnCl_2$, Including a Hand Crushed Mixture.

Figure 4.3 shows the XRD profiles for most SDT analyzed mixtures. The peaks locations were obtained and matched with: $LiBH_4$ [38-40, 46], MgH_2 [65, 78-81], LiCl [46, 82], thin foil (refer to Figure 4.4) and $ZnCl_2$ (refer to Figure 4.5 and PANalytical X'pert Highscore software version 1.0e reference code 00-016-0850).

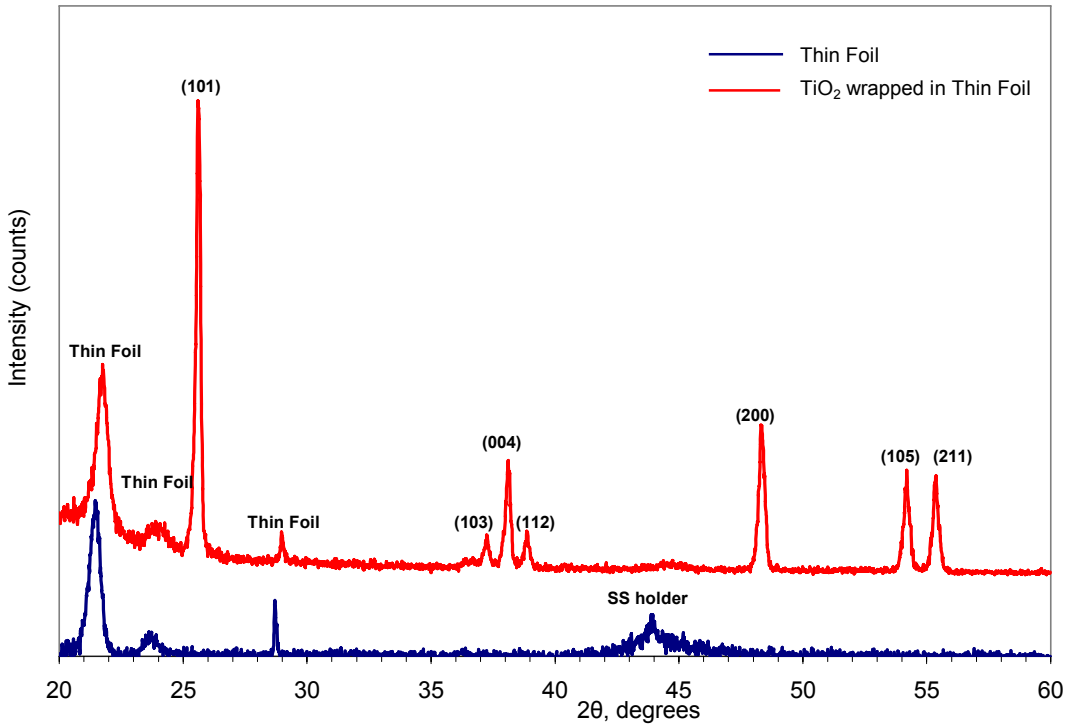

Figure 4.4: XRD Profile for the Polyethylene Clear Plastic Wrap (Thin Foil) Used to Protect the Samples.

It can be corroborated the incomplete reaction for the 10 minute hand mixed sample with the peaks of the reactants present in the mixture. While comparing the hand mixed and ball milled samples analyses, two unknown peaks at around 20^0 and 20.5^0 indicate a possible relationship in the formation of $Zn(BH_4)_2$ in addition to the LiCl peaks observed indicating a $LiBH_4$ reaction with $ZnCl_2$, however further characterization is needed (see also section 4.3, $2LiBH_4 + MgH_2 + X mol\% ZnCl_2$ for comparison). The

presence of LiCl affects the total hydrogen capacity of the mixture by adding a dead weight which is measured by the SDT. No peaks for TiF_3, MgH_2 and Ni were observed possibly due to their low concentration.

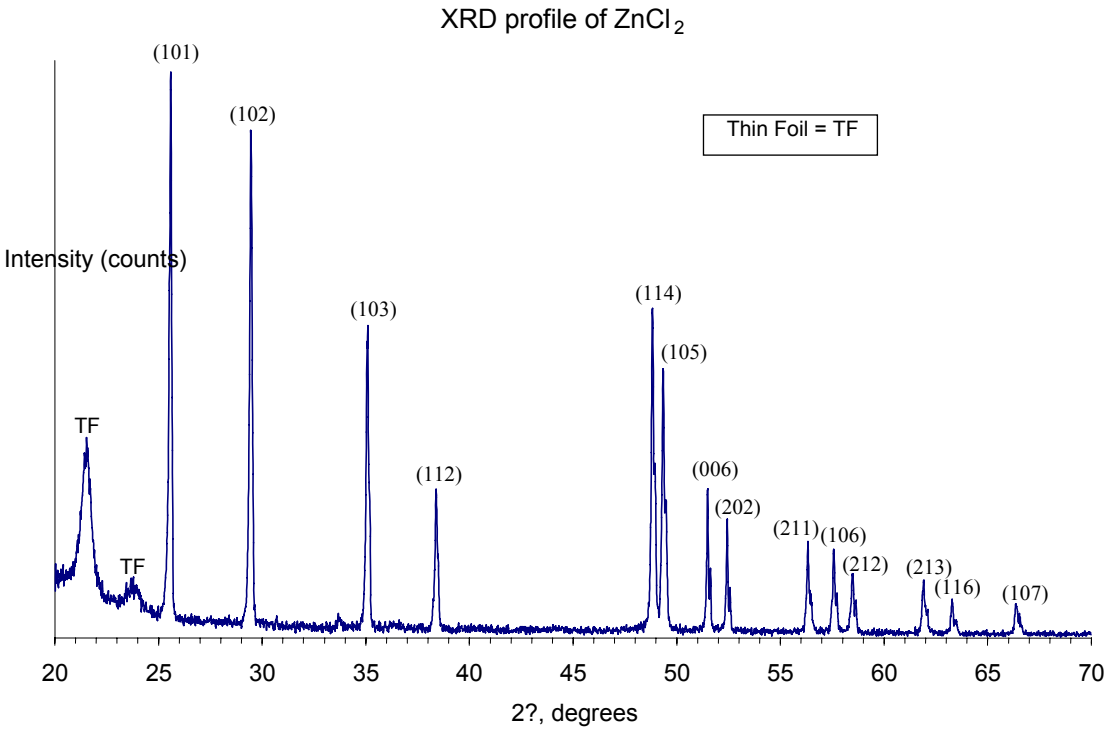

Figure 4.5: XRD Profile of Pure $ZnCl_2$.

4.2 MgH_2 + nanoNi

As part of our investigation, several MgH_2 + nanoX [X=Ni (QuantumSphere) or Zn] mixtures were prepared to study the effects of different nano-metal and dopants for the following mixtures:

(1) $2LiBH_4$ + (MgH_2BM9hrs + 10mol% nanoNi + BM2hr) + BM1hr.

(2) $2LiBH_4$ + MgH_2 + BM1hr.

(3) MgH_2 + 10mol% nanoNi + BM2hrs.

(4) MgH_2BM12hrs.

(5) MgH_2BM9hr + 10mol% nanoZn + BM2hr.

(6) ($2LiBH_4$ + MgH_2BM12hr + BM1hr) + 10mol% nanoNi + BM1hr.

(7) MgH_2 BM9hrs.

(8) MgH_2BM12hr + 5mol% nanoNi + BM1hr.

In Figure 4.6 and 4.9, portions of MgH_2 were ball milled before mixing to lower the desorption temperature and study if further improvements could be achieved by catalytic doping. Previous studies [51, 78, 83, 84] have shown that ball milling reduces MgH_2 desorption temperature. The undoped MgH_2 the sample ball milled for 12 hrs showed a slight reduction in the decomposition temperature at around 325^oC when contrasted with the MgH_2 sample ball milled 9 hrs, both results show lower desorption temperatures than the as-received MgH_2 around 428^0C [85].

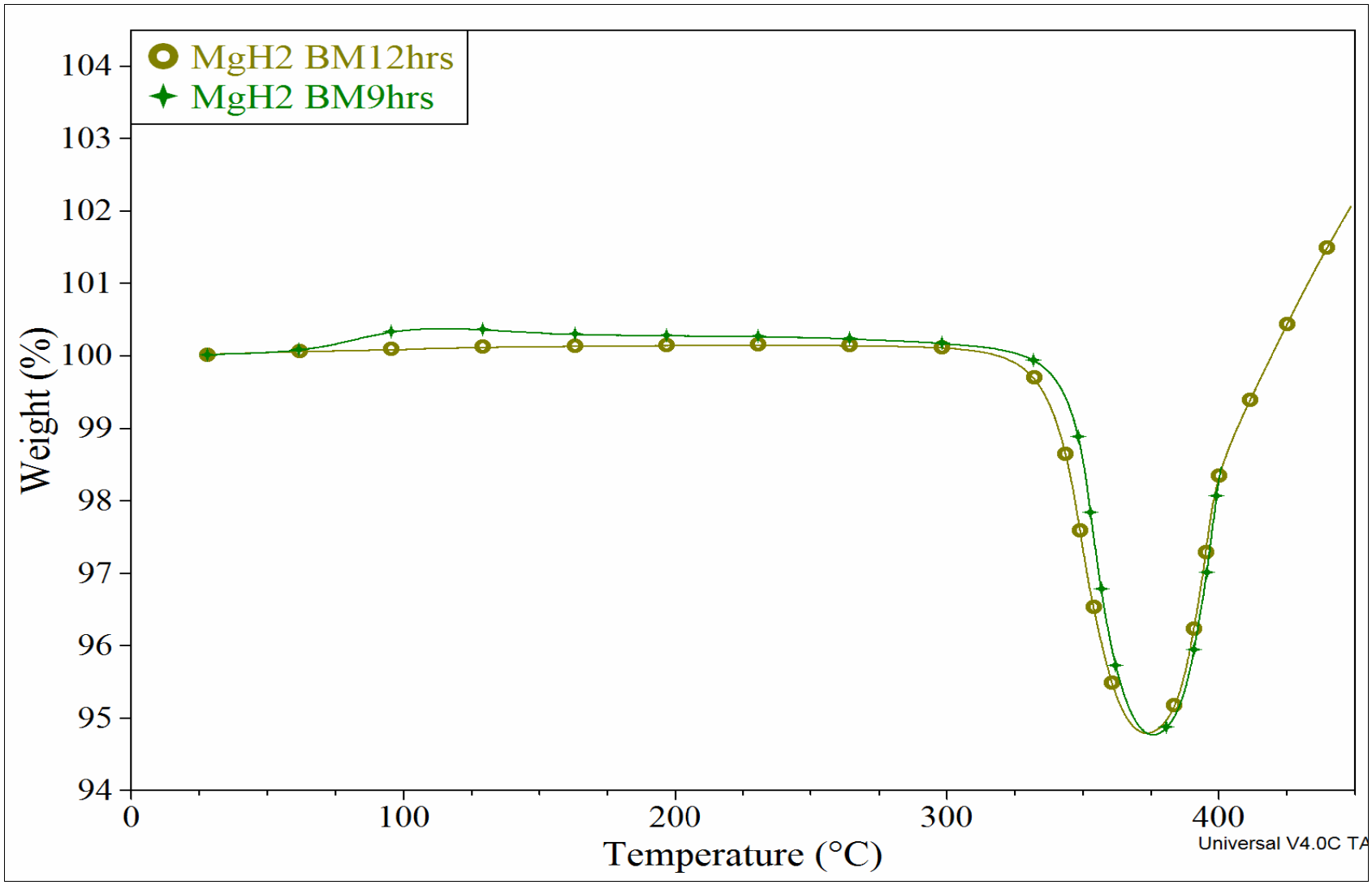

Figure 4.6: SDT-Q600 – TGA Profiles for Undoped MgH_2 + BM9hrs and BM12hrs.

In Figure 4.7 and Figure 4.9, the profiles for mixtures (3), (5) and (8) indicate that samples doped with nanoNi showed a higher effectiveness in reducing the desorption temperature starting at around 225^{o}C when compared with samples doped with nanoZn. The weight loss for doped and undoped MgH_2 samples fluctuated at around 4wt% and 5wt% respectively.

On the other hand, in Figure 4.8 and 4.9, the sample profiles for (1), (2) and (6) show desorption temperatures around 275^{o}C, 350^{o}C and 270^{o}C, respectively. As observed, $2LiBH_4 + MgH_2$ samples doped with nanoNickel exhibits lower dehydrogenation temperatures compared to the undoped counterpart. In addition, total weight losses for the sample profiles (1), (2) and (6) were observed around 3.50wt%, 3.20wt% and 4.66wt%, respectively. The addition of nanoNi influenced the desorption temperatures of MgH_2 by reducing it. Further studies which involve doping $LiBH_4$ with nanoNickel will be carried out.

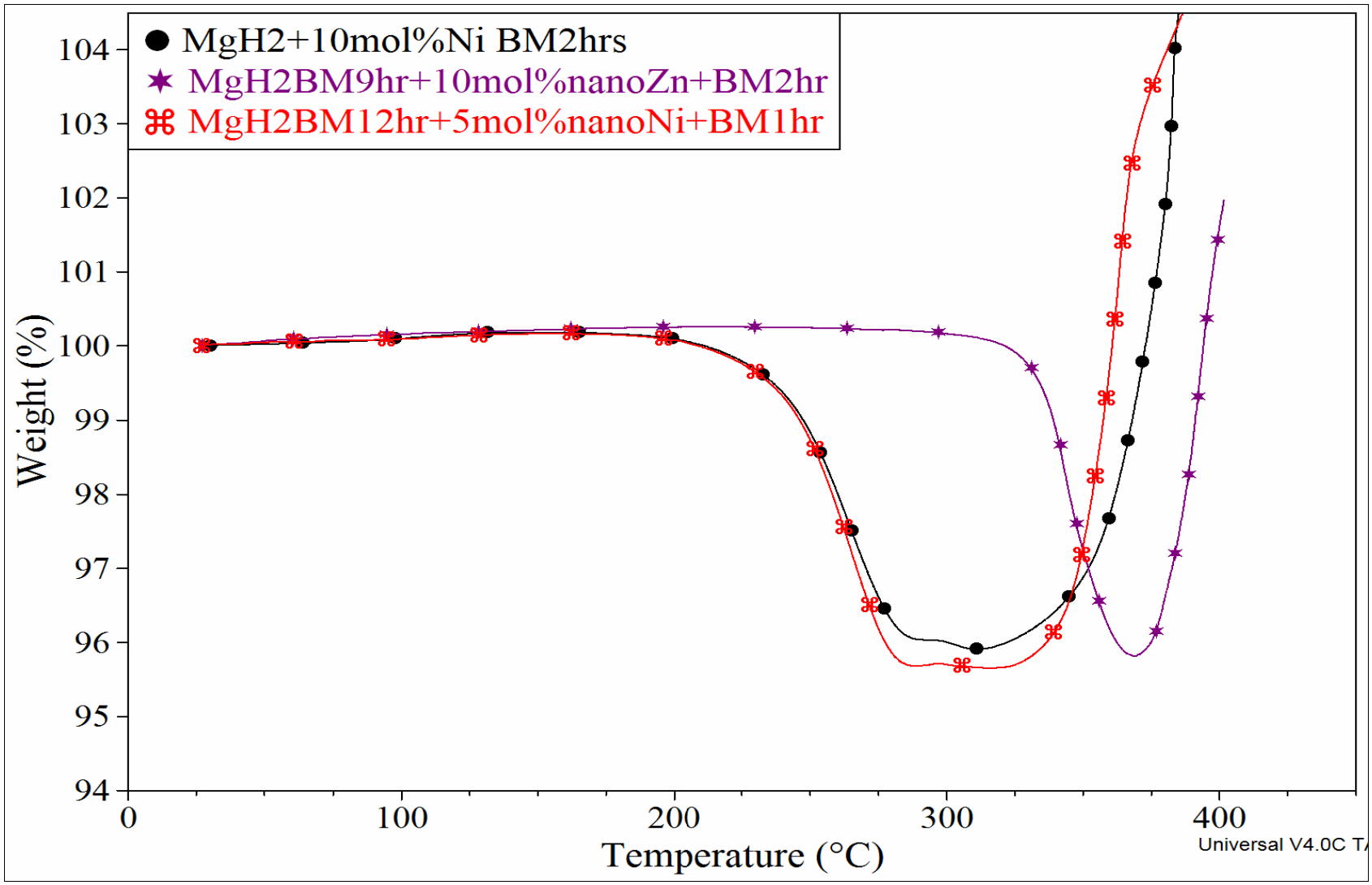

Figure 4.7: SDT-Q600 – TGA Profiles for MgH_2 + nanoNickel.

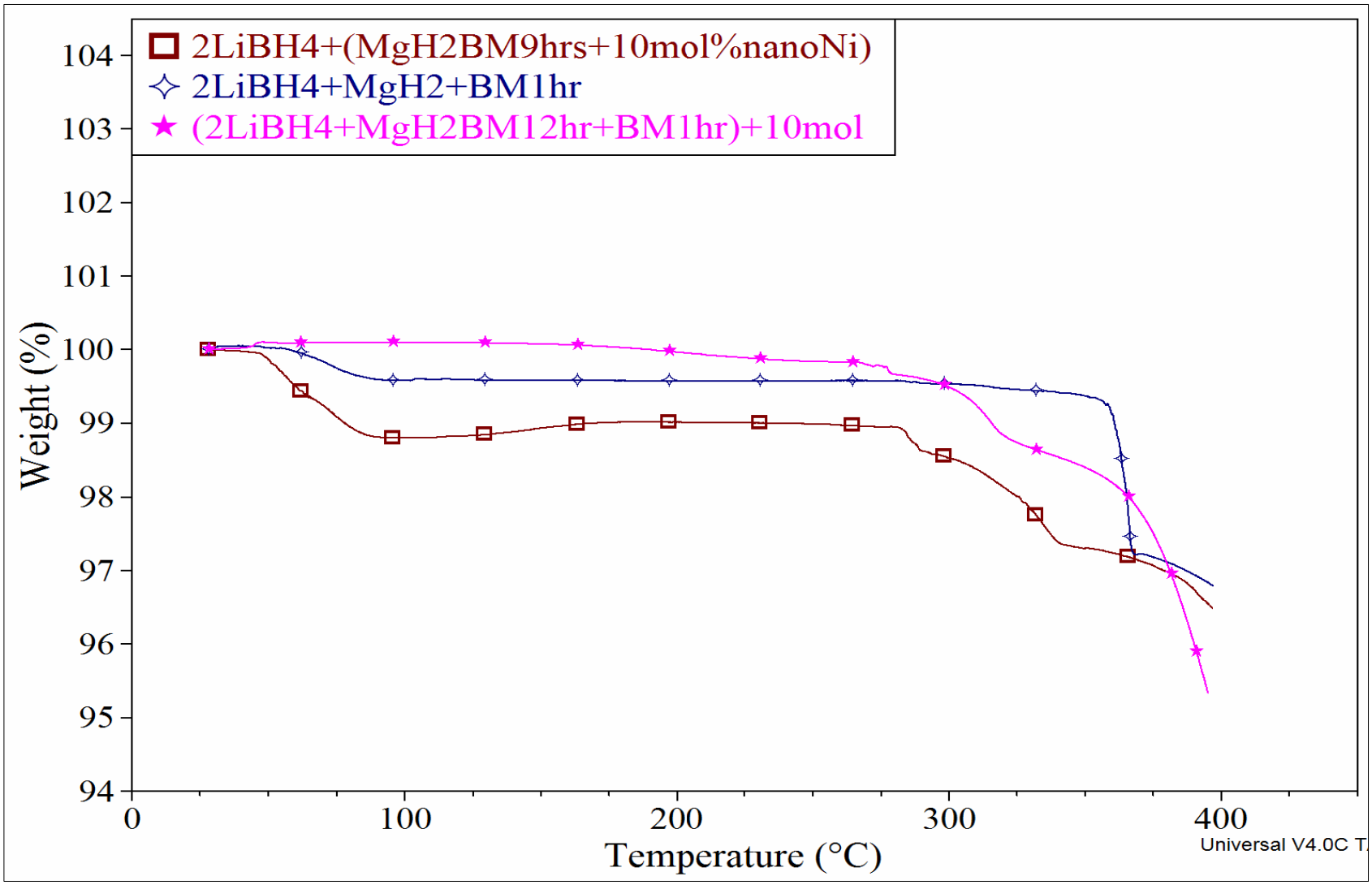

Figure 4.8: SDT-Q600 – TGA Profiles for $LiBH_4/MgH_2$ + nanoNickel.

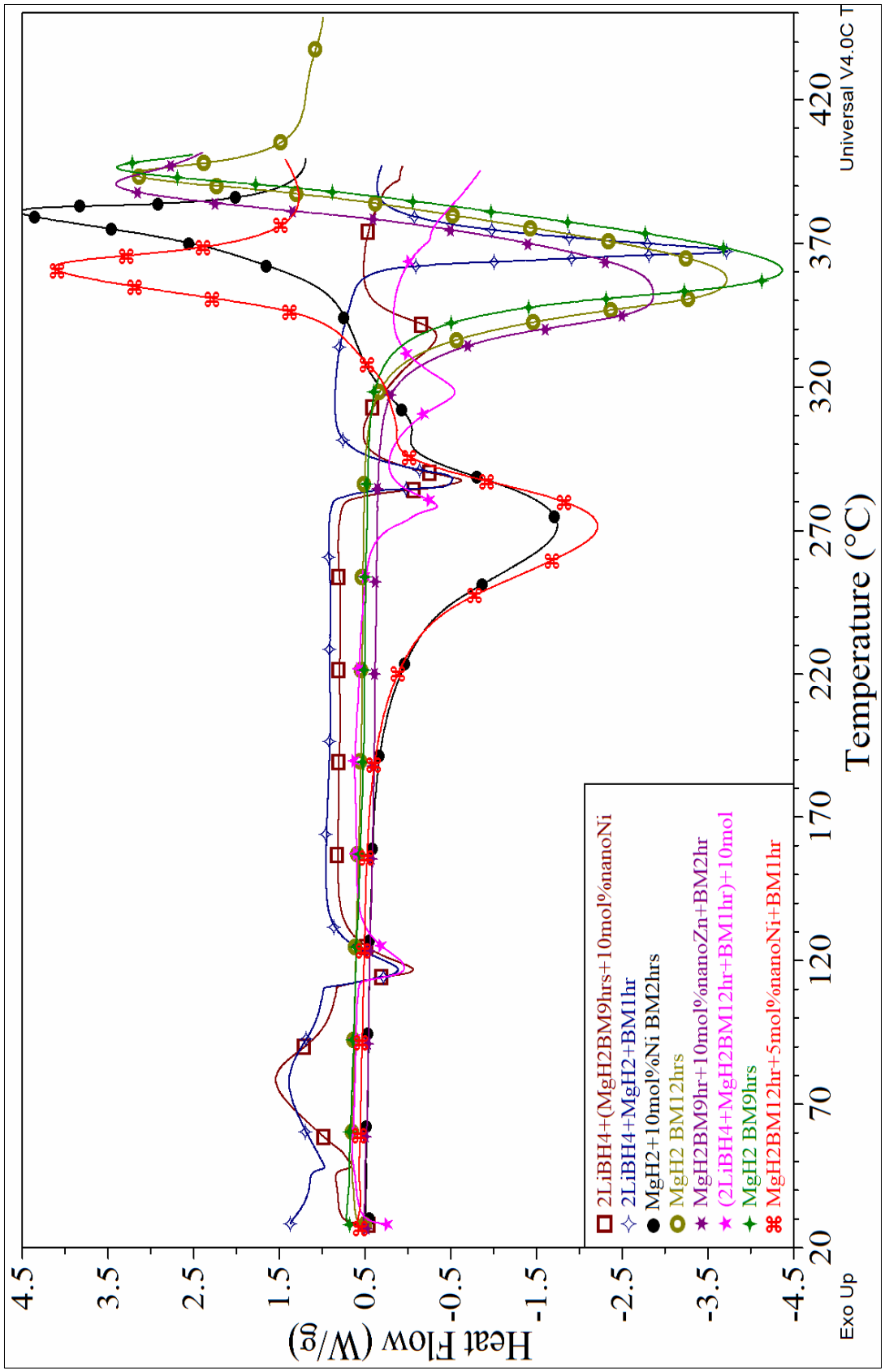

Figure 4.9: SDT-Q600 – DSC Profiles for the Discussed Mixtures in Section 4.2.

4.3 $LiBH_4$ + ½MgH_2 + Xmol% ($ZnCl_2$ or $TiCl_3$)

Figure 4.10 shows different SDT-TGA results for the pristine 95% $LiBH_4$ and mixtures of $LiBH_4$ + ½MgH_2 + Xmol% $ZnCl_2$ (X = 2,4,6,8,10) ball milled for 2 hours under H_2 pressure. A slight weight loss of around 1.2% during the melting process of non-ball milled $LiBH_4$ between the peaks 275-300^oC was observed. A significant exothermic peak around 75^oC with weight loss since the beginning of the analysis [86] indicates a possible hydrolysis [33, 35] of $LiBH_4$ due to moisture. A total weight loss around 13.6wt% was observed for commercial undoped $LiBH_4$.

In addition, a slight shift in the melting peak from approximately 283^oC to 270^oC was observed when contrasting DSC profiles (refer to Figure 4.11) to the non-ball milled $LiBH_4$. This effect could be more associated with the concentration of $ZnCl_2$ than with the ball milling time and/or the addition of MgH_2.

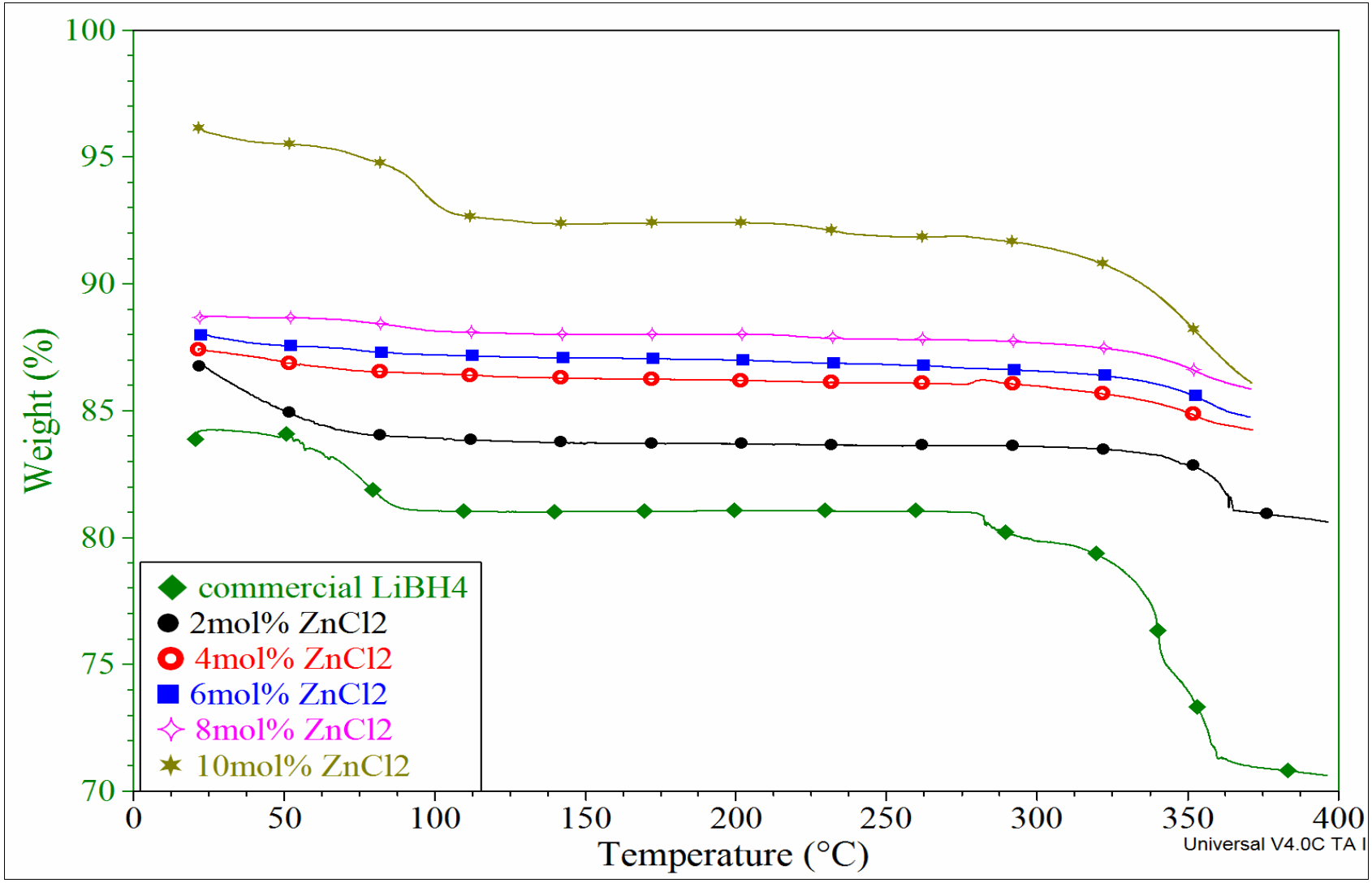

Figure 4.10: SDT-Q600 – TGA Profiles for $LiBH_4$ + ½MgH_2 + 2,4,6,8,10 mol% $ZnCl_2$ Ball Milled for 2 Hours.

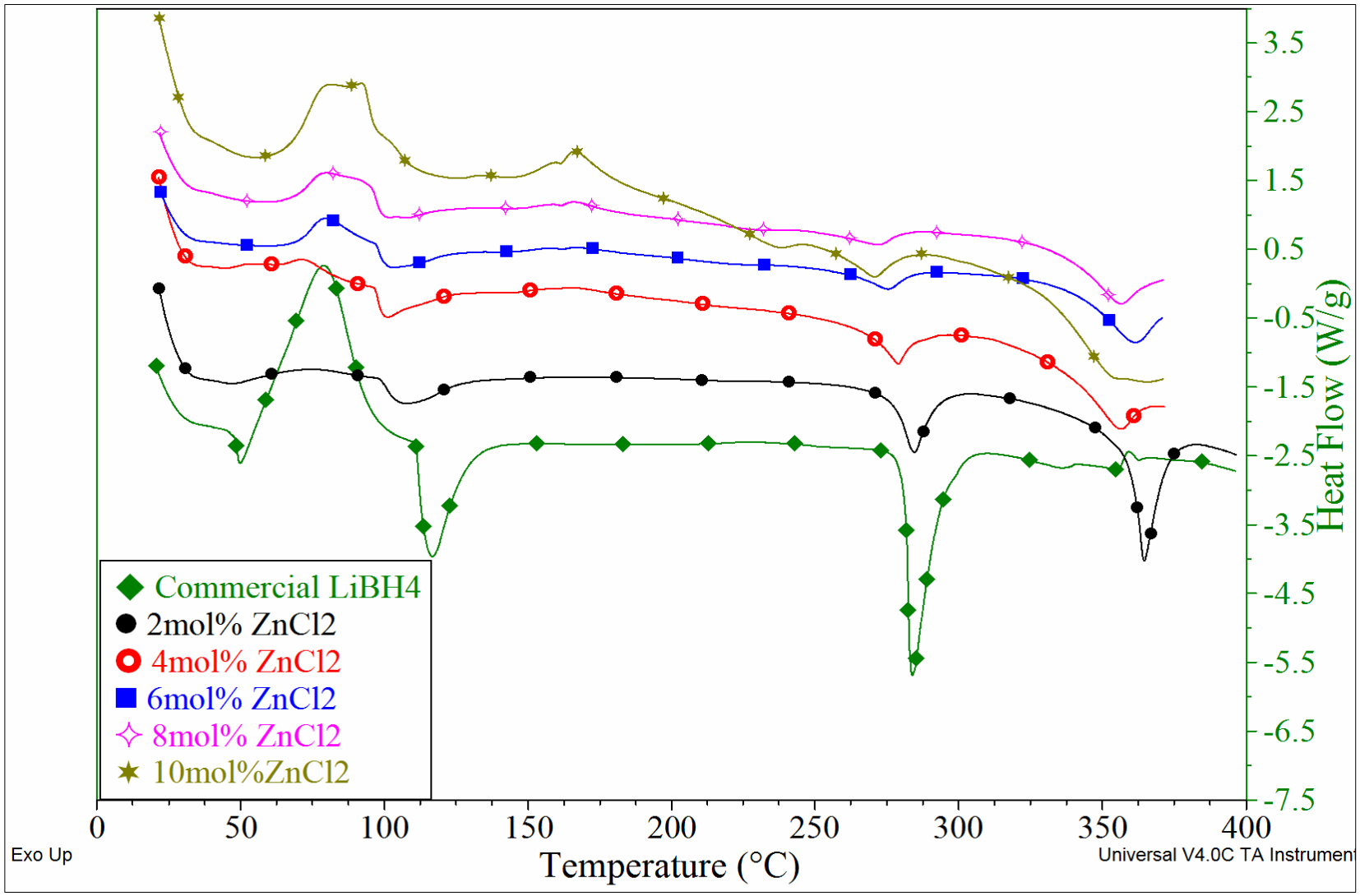

Figure 4.11: SDT-Q600 – DSC Profiles for $LiBH_4$ + ½MgH_2 + 2,4,6,8,10 mol% $ZnCl_2$ Ball Milled for 2 Hours.

According to Figure 4.12, the desorption rate of $LiBH_4 + ½MgH_2$ + 2mol% $ZnCl_2$ ball milled for 2 hours increases with increasing temperature. Desorption rate at 350°C is around 5 times faster than the desorption rate at 300°C. The dramatic desorption difference when comparing the plots for 350°C and 300°C indicates a possible range to locate the significant desorption process, however these high temperatures are not within the DOE FreedomCAR technical targets. An additional observation, assuming the reaction products are: $LiH + ½MgB_2 + 2H_2$, the H_2 total weight percent in the product mixture will decrease with increasing concentration of $ZnCl_2$.

Assuming the later product mixture, for the following $ZnCl_2$ concentrations an approximate theoretical total H_2 weight percentage would be obtained (refer to table 4.2). These weight percentages include the weight of $ZnCl_2$ since it is not eliminated from the mixture. Additional analysis must be performed to the reaction products to determine gas composition.

Table 4.2: Reduction Effect in the Theoretical Total H_2 wt% by $ZnCl_2$ Addition.

Mol% $ZnCl_2$	Total H_2 wt%
2	10.34
4	9.359
6	8.549
8	7.867
10	7.286

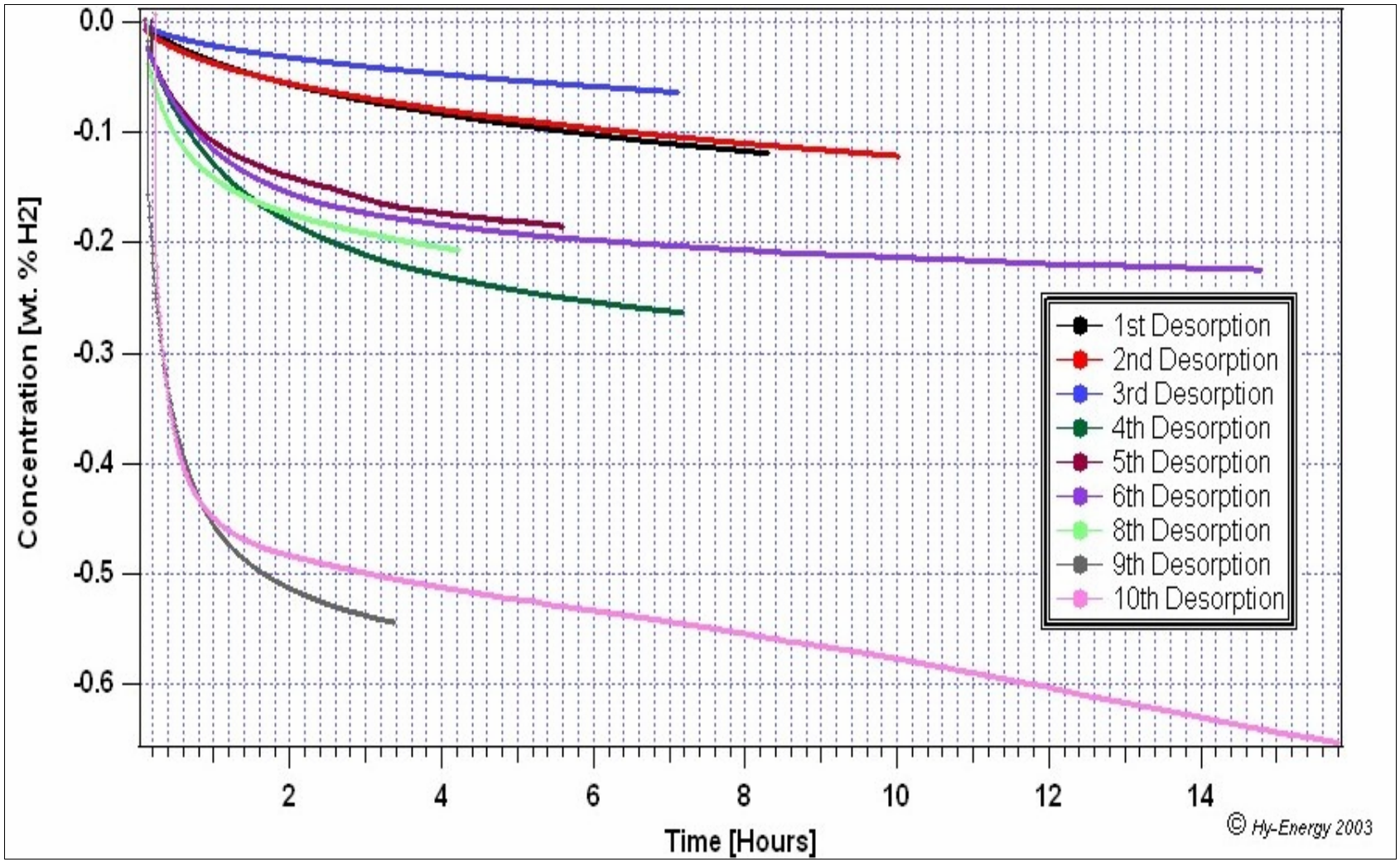

Figure 4.12: Desorption Data Collected on a PCT for $LiBH_4 + ½MgH_2 + 2mol\% ZnCl_2$ Ball Milled 2 Hours Under H_2 Ambient. Desorptions were Performed at Various Temperatures: 1-3 Cycles at 250°C; 4-6 Cycles at 300°C; 8-10 Cycles at 350°C.

The PCT diagram (Figure 4.13), shows two different desorption curves at 250°C and 350°C for $LiBH_4$ + ½MgH_2 + 2mol% $ZnCl_2$ ball milled 2 hours under H_2 pressure. There is no appearance of plateau pressure region for the 1st desorption cycle curve at 250°C which is an indication of no hydrogen being absorbed by the mixture at that temperature. As for the 11th desorption cycle curve at 350°C, a plateau pressure at around 4-5 bars was observed with a total desorption of 1.4 wt.%. It was proven the MgH_2 effects in reducing the reaction enthalpy by 25 kJ/(mol H_2) by destabilizing $LiBH_4$ [46].

The XRD profiles shown in Figure 4.14 correspond to the mixture of $LiBH_4$ + ½MgH_2 + Xmol% $ZnCl_2$ ball milled under an ambient of H_2 gas for 30 minutes. The presence of LiCl and Zn [87] after ball milling for 30 minutes indicates a reaction between $ZnCl_2$ and $LiBH_4$ taking place while the mixture is being pulverized. As stated before in section 4.1, the presence of LiCl affects the overall hydrogen weight loss by adding its dead-weight to the mixture, unless it is removed by purification. In addition, the peak corresponding to LiCl increases with increasing concentration of $ZnCl_2$ while at the same time the relative intensities of peaks corresponding to MgH_2 and $LiBH_4$ decreases. No presence of MgB_2 was found.

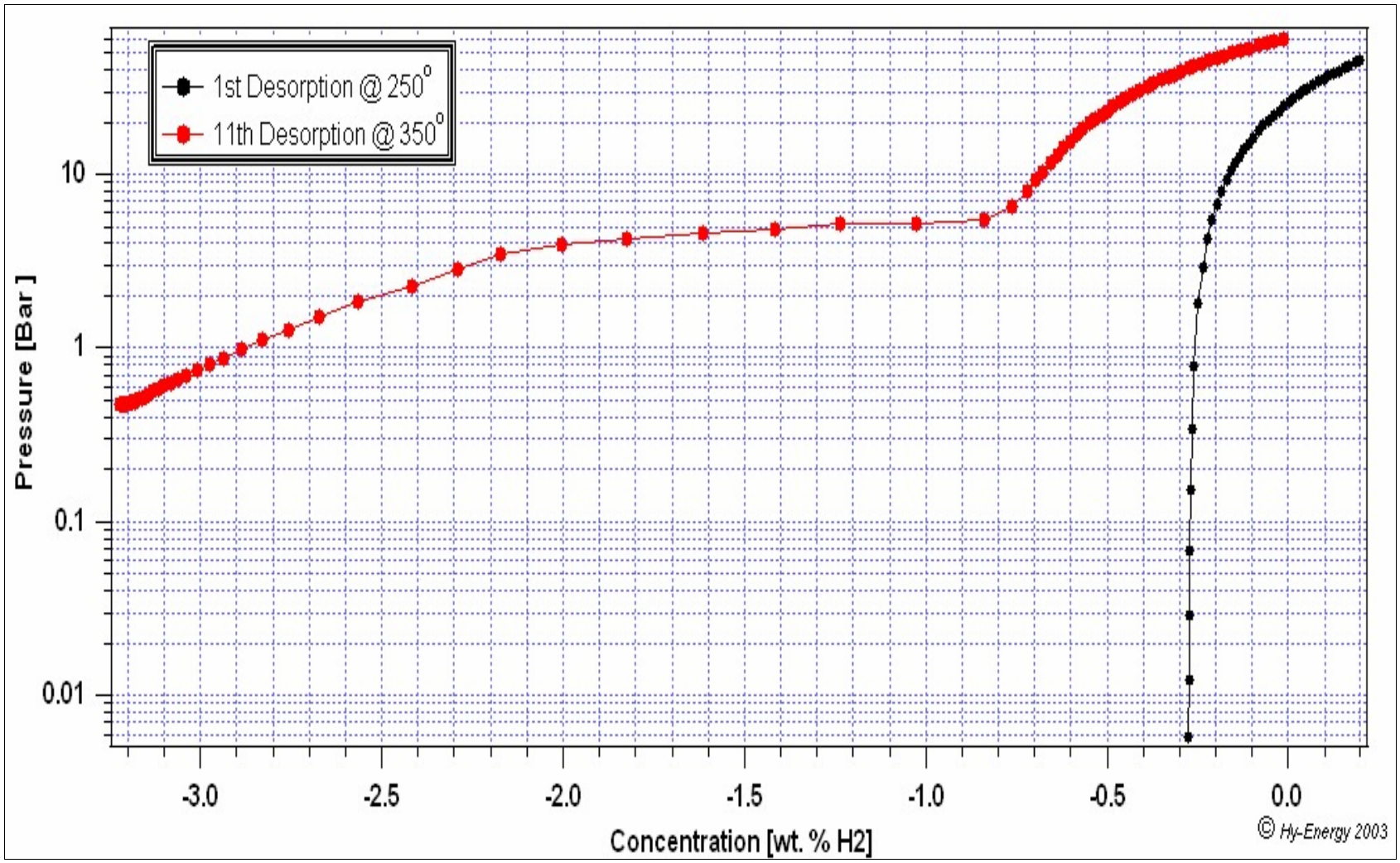

Figure 4.13: PCT Desorption Plots at 250°C and 350°C for the Mixture $LiBH_4$ + ½MgH_2 + 2mol% $ZnCl_2$ Ball Milled 2 Hours Under H_2 Pressure.

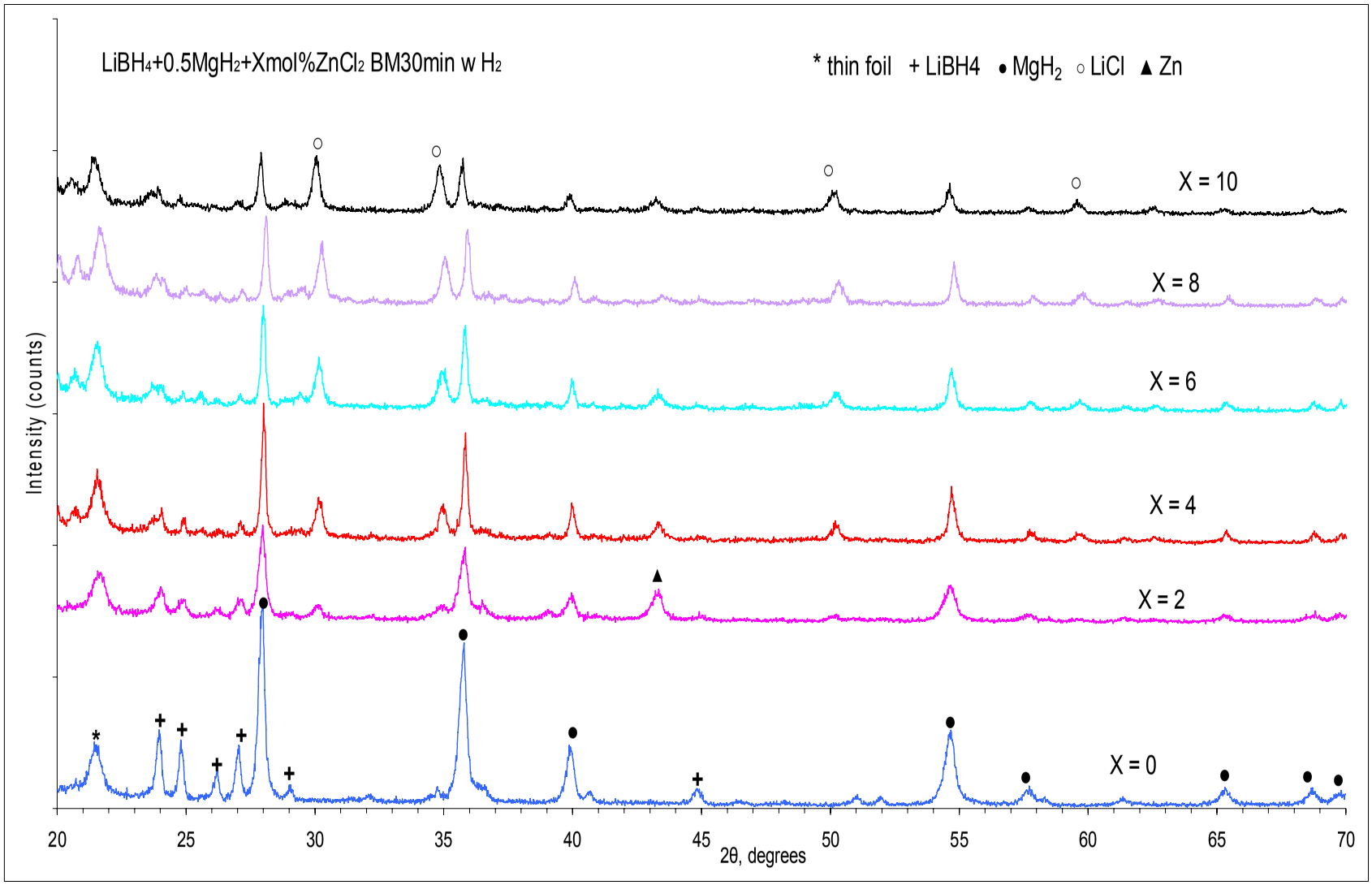

Figure 4.14: XRD Profiles of $LiBH_4$ + ½ MgH_2 + Xmol% $ZnCl_2$ Ball Milled for 30 Minutes Under a H_2 Gas Ambient.

The XRD profiles shown on Figure 4.15 correspond to the mixture of $LiBH_4$ + ½MgH_2 + Xmol% $TiCl_3$ ball milled under an ambient of H_2 gas for 30 minutes. The presence of LiCl after ball milling for 30 minutes indicates a reaction between $TiCl_3$ and $LiBH_4$, possible reaction products could be $Ti(BH_4)_3$ [88] and/or $Ti(BH_4)_4$ (see reference in [18]), however further analyses are needed. Besides, the peak corresponding to LiCl increases with increasing concentration of $TiCl_3$ while at the same time the peaks corresponding to MgH_2 and $LiBH_4$ decreases and no presence of MgB_2 was found.

The FT-IR profiles in Figures 4.16 and 4.17 indicate the B-H stretching for $LiBH_4$ at around 2276 and 2213 cm^{-1} in addition the deformation bands for BH_2 observed at 1118 and 1091 cm^{-1} [89, 90]. There were no other significant peaks that could indicate the presence of additional mixing materials or formation of new compounds.

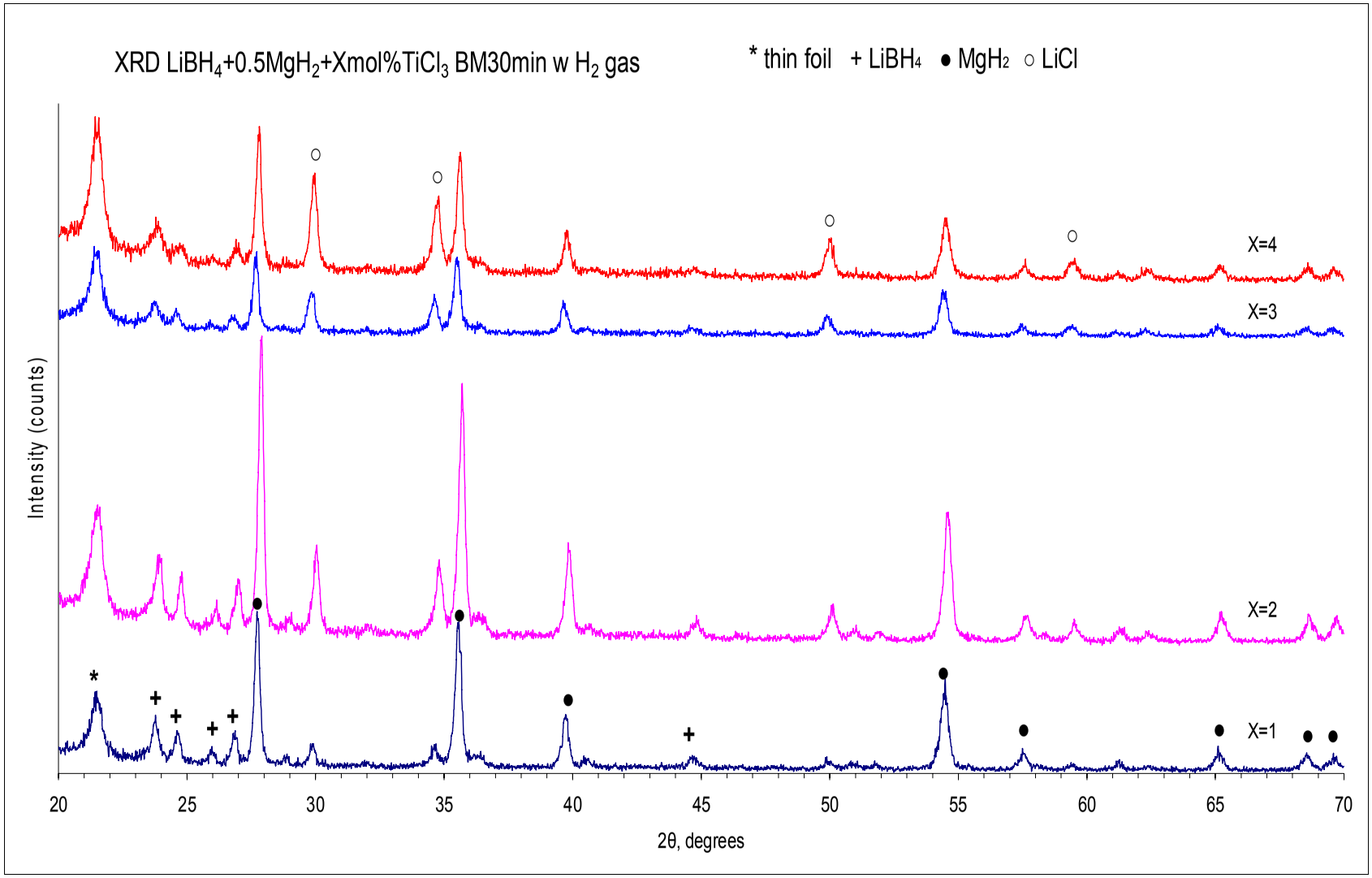

Figure 4.15: XRD Profiles of $LiBH_4$ + ½ MgH_2 + Xmol% $TiCl_3$ Ball Milled for 30 Minutes Under a H_2 Gas Ambient.

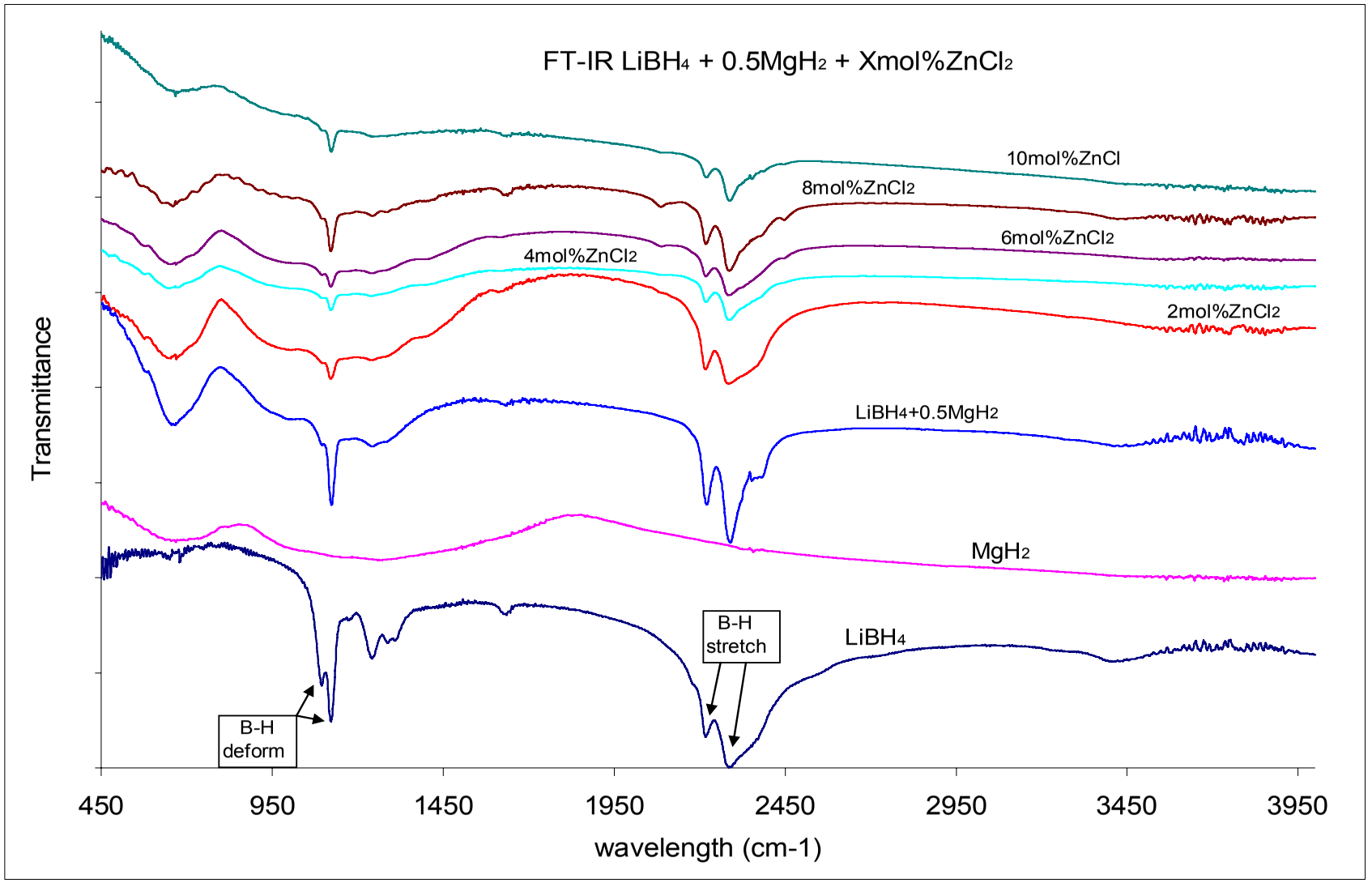

Figure 4.16: FT-IR Profile for $LiBH_4$ + ½ MgH_2 + Xmol% $ZnCl_2$ Ball Milled for 30 Minutes Under a H_2 Gas Ambient.

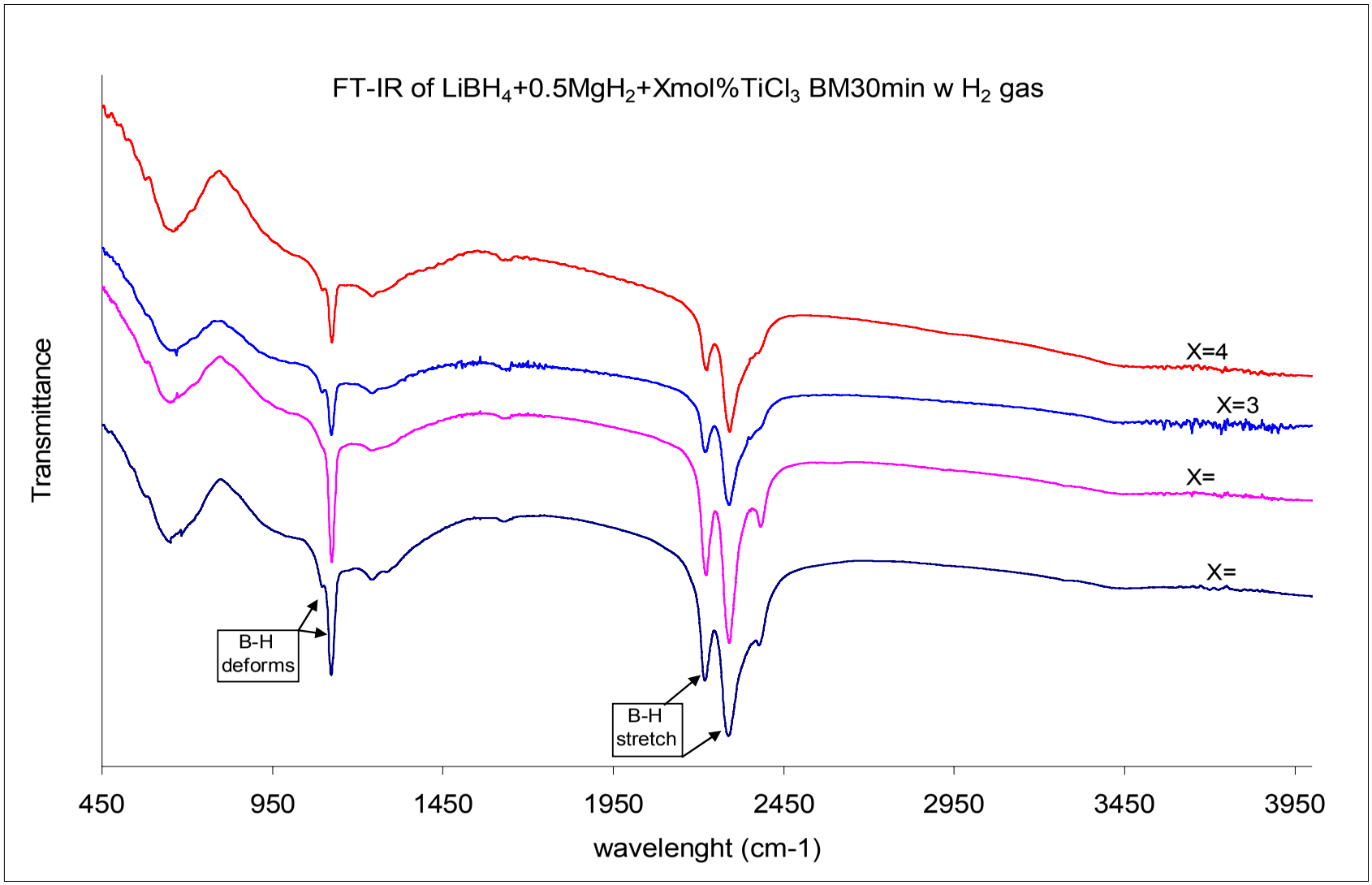

Figure 4.17: FT-IR Profile for $LiBH_4$ + ½ MgH_2 + Xmol% $TiCl_3$ Ball Milled for 30 Minutes Under a H_2 Gas Ambient.

CHAPTER 5

CONCLUSION AND RECOMMENDATIONS

5.1 Conclusion and Recommendations

In summary, the undoped ball milled mixture of $LiBH_4$ / $ZnCl_2$ successfully reduced the desorption temperature close to 100^oC. Doping with nano Nickel demonstrated to further decrease the dehydrogenation temperature. In addition, it was found that $LiBH_4$ + $ZnCl_2$ + 3mol% nanoNi is the optimum mixture for maximum performance. The XRD profiles show LiCl peaks indicating a reaction between $LiBH_4$ and $ZnCl_2$. The weight losses were higher than 10wt%, if assumed that $Zn(BH_4)_2$ is formed during $LiBH_4$ / $ZnCl_2$ ball milling, then, the probabilities of additional compounds being released other than hydrogen are high. It is recommended, for this system, to investigate if there is the presence of $Zn(BH_4)_2$ and to determine gas composition during desorption.

The ball milling process has shown to reduce the desorption temperature of MgH_2. The addition of nanoNickel to MgH_2 has further reduced the dehydrogenation temperature. If adding nanoNickel to the $LiBH_4$ / MgH_2 mixture, the system destabilizes which is indicated by a decrease in the decomposition temperature. However, it is recommended to perform gas composition and thermal equilibrium studies to understand the system.

The mixture of $LiBH_4$ / MgH_2 was successfully prepared by doping with different amounts of $ZnCl_2$ and $TiCl_3$ catalysts. DSC and TGA analysis shows a lower decomposition/melting temperature of $LiBH_4/MgH_2$ mixture in the presence of $ZnCl_2$. The initial rate of hydrogen decomposition from $LiBH_4$ + ½MgH_2 + 2mol% $ZnCl_2$ increases with an increase in temperature. Moreover, the plateau pressure of 4-5 bars at 350^oC indicates a lower energy level for dehydrogenation-rehydrogenation cycling with a volumetric capacity of 3.0wt%, such capacity increases with cycling. The XRD profiles indicate a reaction occurring during the mechano-chemical mixing with $ZnCl_2$ and $TiCl_3$ showing the presence of LiCl as product.

It is recommended to focus the investigation in identifying the possible materials formed besides of LiCl during ball milling and gas composition during desorption process. Identifying the gas composition during desorption might provide useful information regarding the reaction path and products. Further experimental analysis using pressure-composition-isotherms should also be highly considered to identify reversibility.

REFERENCES

1. Energy Information Administration. September 2005. Table 1.3, Energy Consumption by Source, 1949-2005. 2005 Annual Energy Review. DOE/EIA-0384(2005). Washington, DC. (www.eia.doe.gov/emeu/aer).

2. http://www.eia.doe.gov/emeu/ipsr/t21.xls. Found on: February 3, 2007.

3. "Worldwide Look at Reserves and Production," Oil & Gas Journal, Vol. 103, No. 47 (December 19, 2005), pp. 24-25.

4. Energy Information Administration, International Energy Outlook 2006, DOE/EIA-0484(2006) (Washington, DC, June 2006), p. 26.

5. Energy Information Administration, International Energy Outlook 2006, DOE/EIA-0484(2006) (Washington, DC, June 2006), p. 29.

6. Energy Information Administration, International Energy Outlook 2006, DOE/EIA-0484(2006) (Washington, DC, June 2006), p. 26.

7. Energy Information Administration, "A Primer on Gasoline Prices" DOE/EIA-X040 May 2006. (www.eia.doe.gov).

8. Keeling, C. D. *Tellus* 1960, *12*, 200-203.

9. Wilson, Carroll L., and William H. Matthews, Eds. Inadvertent Climate Modification. Report of Conference, Study of Man's Impact on Climate (SMIC), Stockholm. Cambridge, MA: MIT Press. p. 234 (1971).

10. Lorius, C.; Jouzel, J.; Ritz, C.; Merlivat, L.; Barkov, N. I.; Korotkevich, Y. S.; Kotlyakov, V. M. *Nature* 1985, *316*, 591-596.

11. Barnola, J. M.; Raynaud, D.; Korotkevich, Y. S.; Lorius, C. *Nature* 1987, *329*, 408-414.

12. Genthon, G.; Barnola, J. M.; Raynaud, D.; Lorius, C.; Jouzel, J.; Barkov, N. I.; Korotkevich, Y. S.; Kotlyakov, V. M. *Nature* 1987, *329*, 414-418.

13. Energy Information Administration, International Energy Outlook 2006, DOE/EIA-0484(2006) (Washington, DC, June 2006), p. 73.

14. Dresselhaus, M. S.; Thomas, I. L. *Nature* 2001, *414*, 332-337.

15. Crabtree, G. W.; Dresselhaus, M. S.; Buchanan, M. V. *Physics Today* 2004, *57*, 39-44.

16. Schlapbach, L.; Zuttel, A. *Nature* 2001, *414*, 353-358.

17. http://www.eere.energy.gov/hydrogenandfuelcells/fuelcells/fc_types.html.

18. Grochala, W.; Edwards, P. *Chem. Rev.* 2004, *104*, 1283-1315.

19. Renaudin, G.; Guénée, L.; Yvon, K. *J. Alloys Compd*. 2003, *350*, 145-150.

20. Huang, B.; Yvon, K.; Fischer, P. *J. Alloys Compd*. 1994, *210*, 243-246.

21. US Department of Energy, *Basic Research Needs for the Hydrogen Economy: Report of the Basic Energy Sciences Workshop on Hydrogen Production, Storage and Use*. May 13-15, 2003. p. 35.

22. US Department of Energy, *Basic Research Needs for the Hydrogen Economy: Report of the Basic Energy Sciences Workshop on Hydrogen Production, Storage and Use*. May 13-15, 2003. p. 31.

23. http://www1.eere.energy.gov/hydrogenandfuelcells/storage/pdfs/targets_onboard_hydro_storage.pdf.

24. U.S. Department of Energy, *Hydrogen Storage "Think Tank" Report*; March 14th, 2003; Washington, D.C.

25. Dillon, A. C.; Jones, K. M.; Bekkedahl, T. A.; Kiang, C. H.; Bethune, D. S.; Heben, M. J. *Nature* 1997, *386*, 377-379.

26. Wang, S.; Li, G. Q.; Millar, G. J. *Energy & Fuels* 1996, *10*, 896-904.

27. US Department of Energy, *Basic Research Needs for the Hydrogen Economy: Report of the Basic Energy Sciences Workshop on Hydrogen Production, Storage and Use*. May 13-15, 2003. p. 41.

28. Bogdanovic, B.; Schwickardi, M. *J. Alloys Compd*. 1997, *253-254*, 1-9.

29. Zaluska, A.; Zaluski, L.; Strom-Olsen, J. O. *J. Alloys Compd*. 2000, *298*, 125-134.

30. Fichtner, M.; Engel, J.; Fuhr, O.; Kircher, O.; Rubner, O. *Materials Science & Engineering, B: Solid-State Materials for Advanced Technology* 2004, *B108*, 42-47.

31. Srinivasan, S. S.; Brinks, H. W.; Hauback, B. C.; Sun, D.; Jensen, C. M. *J. Alloys Compd.* 2004, *377*, 283-289.

32. Sun, D.; Srinivasan, S. S.; Chen, G.; Jensen, C. M. *J. Alloys Compd*. 2004, *373*, 265-269.

33. Schlesinger, H. I.; Brown, H. C.; Finholt, A. E.; Gilbreath, J. R.; Hoekstra, H. R.; Hyde, E. K. *J. Am. Chem. Soc*. 1953, *75*, 215-219.

34. Kong, V. C. Y.; Foulkes, F. R.; Kirk, D. W.; Hinatsu, J. T. *Int. J. Hydrogen Energy* 1999, *24*, 665-675.

35. Kojima, Y.; Kawai, Y.; Kimbara, M.; Nakanishi, H.; Matsumoto, S. *Int. J. Hydrogen Energy* 2004, *29*, 1213-1217.

36. Schlesinger, H. I.; Brown, H. C. *J. Am. Chem. Soc*. 1940, *62*, 3429-35.

37. Fedneva, E. M.; Alpatova, V. L.; Mikheeva, V. I. *Russ. J. Inorg. Chem*. 1964, *9*, 826-827.

38. Zuttel, A.; Wenger, P.; Rentsch, S.; Sudan, P.; Mauron, Ph.; Emmenegger, Ch. *J. Power Sources* 2003, *118*, 1-7.

39. Zuttel, A.; Rentsch, S.; Fischer, P.; Wenger, P.; Sudan, P.; Mauron, Ph.; Emmenegger, Ch. *J. Alloys Compd*. 2003, *356-357*, 515-520.

40. Orimo, S.; Nakamori, Y.; Kitahara, G.; Miwa, K.; Ohba, N.; Towata, S.; Zuttel, A. *J. Alloys Compd*. 2005, *404-406*, 427-430.

41. Harris, P. M.; Meibohm, E. B. *J. Am. Chem. Soc*. 1947, *69*, 1231.

42. Gomes, S.; Hagemann, H.; Yvon, K. *J. Alloys Compd*. 2002, *346*, 206.

43. Soulié, J.-Ph.; Renaudin, G.; Cerný, R.; Yvon, K. *J. Alloys Compd*. 2002, *346*, 200.

44. Hagemann, H.; Gomes, S.; Renaudin, G.; Yvon, K. *J. Alloys Compd*. 2004, *363*, 129.

45. Stasinevich, D. S.; Egorenko, G. A. *Russ. J. Inorg. Chem*. 1968, *13*, 341-343.

46. Vajo, J. J.; Skeith, S. L.; Mertens, F. *J. Phys. Chem. B* 2005, *109*, 3719-3722.

47. Chen, Y.; Williams, J. S. *J. Alloys Compd*. 1995, *217*, 181.

48. Tessier, P.; Enoki, H.; Bououdina, M.; Akida, E. *J. Alloys Compd*. 1998, *268*, 285.

49. Huot, J.; Akida, E.; Takada, T. *J. Alloys Compd*. 1995, *231*, 815.

50. Zaluska, A.; Zaluski, L.; Ström-Olsen, J. O. *J. Alloys Compd*. 1999, *288*, 217.

51. Gennari, F. C.; Castro, F. J.; Urretavizcaya, G. *J. Alloys Compd*. 2001, *321*, 46-53.

52. Zaluski, L.; Zaluska, A.; Tessier, P.; Stroem-Olsen, J. O.; Schulz, R. *J. Alloys Compd*. 1995, *227*, 53-57.

53. Liang, G.; Boily, S.; Huot, J.; Van Neste, A.; Schulz, R. *J. Alloys Compd*. 1998, *268*, 302-307.

54. Liang, G.; Boily, S.; Huot, J.; Van Neste, A.; Schulz, R. *J. Alloys Compd*. 1998, *267*, 302-306.

55. Gross, K. J.; Spatz, P.; Zuttel, A.; Schlapbach, L. *J. Alloys Compd*. 1996, *240*, 206-213.

56. Barkhordarian, G.; Klassen, T.; Bormann, R. *Scripta Mater*. 2003, *49*, 213.

57. Barkhordarian, G.; Klassen, T.; Bormann, R. *J. Alloys Compd*. 2004, *364*, 242.

58. Liang, G.; Huot, J.; Boily, S.; Van Neste, A.; Schulz, R. *J. Alloys Compd*. 1999, *291*, 295-299.

59. Liang, G.; Huot, J.; Boily, S.; Van Neste, A.; Schulz, R. *J. Alloys Compd*. 1999, *292*, 247-252.

60. Liang, G.; Huot, J.; Boily, S.; Schulz, R. *J. Alloys Compd*. 2000, *305*, 239-245.

61. Dehouche, Z.; Djaozandry, R.; Huot, J.; Boily, S.; Goyette, J.; Bose, T. K.; Schulz, R. *J. Alloys Compd*. 2000, *305*, 264-271.

62. Huot, J.; Pelletier, J. F.; Liang, G.; Sutton, M.; Schulz, R. *J. Alloys Compd*. 2002, *330-332*, 727-731.

63. Reilly, J. J.; Sandrock, G. D. *Scientific American* 1980, *242*, 98.

64. Douglass, D. L. *Metall. Trans. A* 1975, *6A*, 2179.

65. Cooper, D.; Wu, C. Y.; Yasensky, D.; Butt, D.; Cai, M. *KONA* 2005, *23*, 139-151.

66. Marks, T. J.; Kolb, J. R. *Chem. Rev*. 1977, *77*, 263.

67. Jeon, E.; Cho, Y.W. *J. Alloys Compd*. 2006, *422*, 273-275.

68. http://www.gloveboxes.com/glove-box-systems.htm.

69. Diagram found inside TA Instruments System One User Manual, p. 33.

70. http://www.fritsch.de/entry.php?page=messe&ulang=2&uid=45f75a6dc3f32cecdb50d7845143c1f7e2833c99278e794f.

71. http://www.fritsch.de/data/manuals/ba_062000_1336_e.pdf. Operating Instructions Planetary Mono Mill "pulverisette 6".

72. Diagrams found on the "SDT online help" software which is included with the SDT Q600 model.

73. http://www.3me.tudelft.nl/live/binaries/5f016600-69e9-4978-bbd3-173bc0136f91/img/TGA%202.jpg.

74. http://en.wikipedia.org/wiki/Image:Loi_de_bragg.png.

75. http://pubs.usgs.gov/of/2001/of01-041/htmldocs/xrpd.htm.

76. PCTPro-2000 Installation and Operation Manual, Hy-Energy LLC.

77. http://ocw.mit.edu/NR/rdonlyres/Chemistry/5-32Intermediate-Chemical-ExperimentationSpring2003/CA6722BA-7333-4A99-B4AB-1F7B880080C6/0/Appendix_1_Qual_Instrumentation_03.pdf.

78. Shang, C. X.; Guo, Z. X. *J. Power Sources* 2004, *129*, 73-80.

79. Hanada, N.; Ichikawa, T.; Fujii, H. *J. Phys. Chem. B* 2005, *109*, 7188-7194.

80. Huang, Z. G.; Guo, Z. P.; Calka, A.; Wexler, D.; Lukey, C.; Liu, H. K. *J. Alloys Compd*. 2006, *422*, 299-304.

81. Jensen, T. R.; Andreasen, A.; Vegge, T.; Andreasen, J. W.; Stahl, K.; Pedersen, A. S.; Nielsen, M. M.; Molenbroek, A. M.; Besenbacher, F. *Int. J. Hydrogen Energy* 2006, *31*, 2052-2062.

82. Obtained from the software PANalytical X'pert Highscore software version 1.0e. Reference code: 00-004-0664. Primary reference: Swanson, Tatge., *Natl. Bur. Stand. (U.S.), Circ. 539*, I, 62, (1953).

83. Hanada, N.; Ichikawa, T.; Orimo, S.; Fujii, H. *J. Alloys Compd*. 2004, *366*, 269-273.

84. Barkhordarian, G.; Klassen, T.; Bormann, R. *J. Phys. Chem. B* 2006, *110*, 11020-11024.

85. Czujko, T.; Varin, R. A.; Wronski, Z.; Zaranski, Z.; Durejko, T. *J. Alloys Compd*. 2007, *427*, 291-299.

86. Slattery, D. K.; Hampton, M. D. Proceedings of the 2002 US DOE Hydrogen Program Review NREL/CP-610-32405.

87. Obtained from the software PANalytical X'pert Highscore software version 1.0e. Reference code: 00-004-0831. Primary reference: Swanson, Tatge., *Natl. Bur. Stand. (U.S.), Circ. 539*, I, 16, (1953).

88. Hoekstra, H. R.; Katz, J. J. *J. Am. Chem. So*c. 1949, *71*, 2488-92.

89. Chater, P. A.; David, W. I. F.; Johnson, S. R.; Edwards, P. P.; Anderson, P. A. *Chem. Commun*. 2006, 2439.

90. Johnson, S. R.; Anderson, P. A.; Edwards, P. P.; Gameson, I.; Prendergast, J. W.; Al-Mamouri, M.; Book, D.; Harris, I. R.; Speight, J. D.; Walton, A. *Chem. Comm*. 2005, 2823-2825.